Chapter 3

Quinolones interacting with copper (II), nickel (II), Vanadium (II), Manganese (II) and zinc (II): structural features, biological evaluation and perspectives

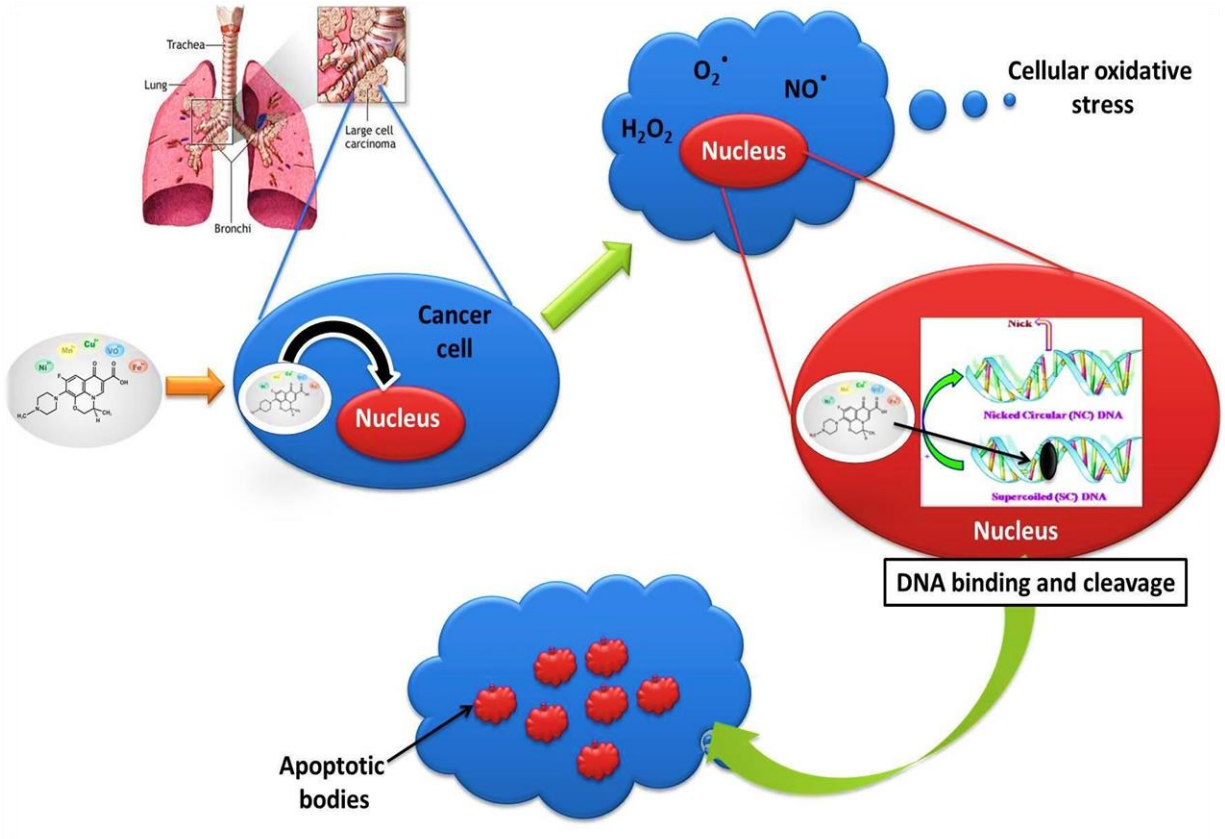

3.1 Introduction

Lung cancer is the most frequently diagnosed malignancy throughout the world and its global incidence is increasing primarily due to increase in cigarette smoking habits. In China it is the top of 10 malignant neoplasms. Similarly, lung cancer is by far the leading cause of cancer death among both men and women in the United States, which will be an estimated 1,658,370 deaths in 2015 accounting for about 28% of all cancer deaths [1], of these, non-small cell lung cancer (NSCLC) accounted for ~85%. Despite improved methods of lung cancer detection and technical advances in treatment modalities, it is found that the efficacy of different anticancer agents for treating advanced stages of lung cancer is limited. It has also been reported that non-small cell lung cancer carcinoma (NSCLC) shows relative resistance to anti-cancer drugs and radiation treatment with respect to small cell lung carcinoma (SCLC) [2]. Thus, search for new drugs with potential antitumor activity in treating lung cancer is needed.

The development of metal complexes as artificial nucleases is an area of burgeoning interest. The metal complexes as pharmaceuticals have gained access over traditional drugs containing organic moieties, due to their potential use as regulators of gene expression and tools of molecular biology [3].The major intracellular target of anticancer metallodrugs is DNA; therefore metal complexes that can bind to specific nucleotides of DNA are of interest. Studies of metal complexes, which react at specific sites along a DNA strand, provide routes toward the rational development of chemotherapeutic agents, sensitive chemical probes for DNA structure in solution and tools for the molecular biologist to dissect genetic systems. In this regard, transition metal complexes are outstanding as artificial nuclease for DNA due to their diverse ability to recognize and react selectively with individual target sites [4]. This has

stimulated considerable interest in searching for new metal complexes as modern therapeutics, diagnostic and radiopharmaceutical agents.

Fluoroquinolones (FQs), with a quinolone main ring and an aminoalkyl substituent are known DNA damaging antibacterial agents. This family of compounds develops its pharmacological activity preventing the replication and repair of bacterial DNA by the DNA gyrase (topoisomerase II) enzyme [5]. During the past years, the antitumoral activity of some FQs has raised much attention [6].In vitro and in vivo studies have confirmed the anticancer effects of these drugs supported by the reduction of all-cause mortality among cancer patients [7]. The FQ antitumor effect has been associated with the inhibition of mammalian DNA topoisomerase I, topoisomerase II, and DNA polymerase. Certain key advantages of fluoroquinolone therapy include facile penetration into inflammatory fluids and attainment of higher concentration in the cell than serum levels, concentration of fluoroquinolones in the lung reaches around 4-fold higher than serum levels.

Moxifloxacin (MFL) [(1'S,6'S)-1-Cyclopropyl-7-(2,8 diazabicyclo[4.3.0] non-8-yl)-6-fluoro-8-methoxy-4-oxo-1,4-dihydroquinoline-3-carboxylic acid] is a 3rd generation fluroquinolone drug, used for the treatment of acute exacerbations of chronic bronchitis (AECB), community acquired pneumonia (CAP), acute bacterial sinusitis and skin infections. It has a broad spectrum of antibacterial properties including the one against penicillin resistant *Streptococcus pneumonia* and thus is an important option in the treatment of bacterial infections [10]. MFL is a DNA gyrase (topoisomerase-II) inhibitor; which is a marker of cell proliferation in normal as well as cancerous tissues [11]. DNA gyrase is an essential bacterial enzyme that maintains the supercoiled structure of DNA and is required for DNA repair, transcription, recombination and transposition, inhibition of DNA gyrase is bactericidal.

Levofloxacin(LFL),[9-fluoro-2.3-dihy-ρ-3-methyl-10-(4-methyl-1-piperazinyl)-7-oxo7H-

pyrido (1,2,3-de)-1,4-benzoxazine-6-carboxylic acid] considered by some authors as a second generation fluoroquinolone on the basis of its' chemical structure [11], has been considered by others as a third-generation quinolone on the basis that although it displays similar activity against Gram-negative species as ciprofloxacin (the second generation fluoroquinolone with the strongest potency) it is twice as active against Gram-positive bacteria [12]. This chiral fluorinated carboxyquinolone is the L-isomer of the second generation racemate ofloxacin. It is commonly used in genitourinary, respiratory and gastrointestinal tracts as well as skin and soft tissue' infections [13].

Due to their wide use, there has been an increasing menace of bacterial resistance to quinolones, which led to the need to improve existing antimicrobial drugs and/or develop new ones, pushing forward the concept that metal complexes could be an alternative to conventional drugs, as novel derivatives of FQ's. Metal complexation has been suggested to play an important role in the biological activities of quinolone compounds [8]. Metal co-ordination to the drug molecules can be used as a strategy to enhance their activity and overcome resistance. A large number of studies have been described in the literature between various quinolone derivatives and metal ions [9], though a thorough survey of literature on antitumor activities of metal-fluoroquinolates has revealed only a limited number of studies on A549 cells.

This present work stems from our interest to develop transition-metal complexes as artificial metallonucleases /metalloantibiotics. In present study, interaction of Cu^{2+}, Fe^{3+}, Mn^{2+}, Ni^{2+}, Zn^{2+}, and VO^{2+} with the FQ's (MFL,LFL) has been studied in order to examine the binding mode and the biological properties of the complexes. The resultant neutral mononuclear complexes of FQ's have been synthesized and characterized by various physicochemical methods. The binding properties of the complexes with CT-DNA have been investigated with UV and CV titrations. Competitive binding studies

with ethidium bromide (EB) have been employed in order to investigate a potential binding mode. The affinity of the complexes for bovine serum albumin (BSA), responsible for the transport of drugs in the body, has been investigated with fluorescence spectroscopy. Considering the growth inhibitory potentialities of some fluroquinolones on certain neoplastic cells, the antiproliferative and apoptotic activity of the synthesized metal complexes have been investigated on A549 cells. The antibacterial activity of the complexes has been evaluated by determining the zone of inhibition (ZI) against four microorganisms.

3.2 General synthesis of complexes

Methanolic solution of Moxifloxacin (MFL)/ Levofloxacin (LFL) (1.0 mmol) in presence of KOH (1.0 mmol) was added dropwise to a methanolic solution of the metal salt (1.0 mmol). The pH was adjusted to ~6.0 (Scheme 3.1). The resulting solution was refluxed for 6 hour on a steam bath, followed by concentrating it to half of its original volume. A fine amorphous product obtained was washed with ether/hexane and dried in vacuum desiccator.

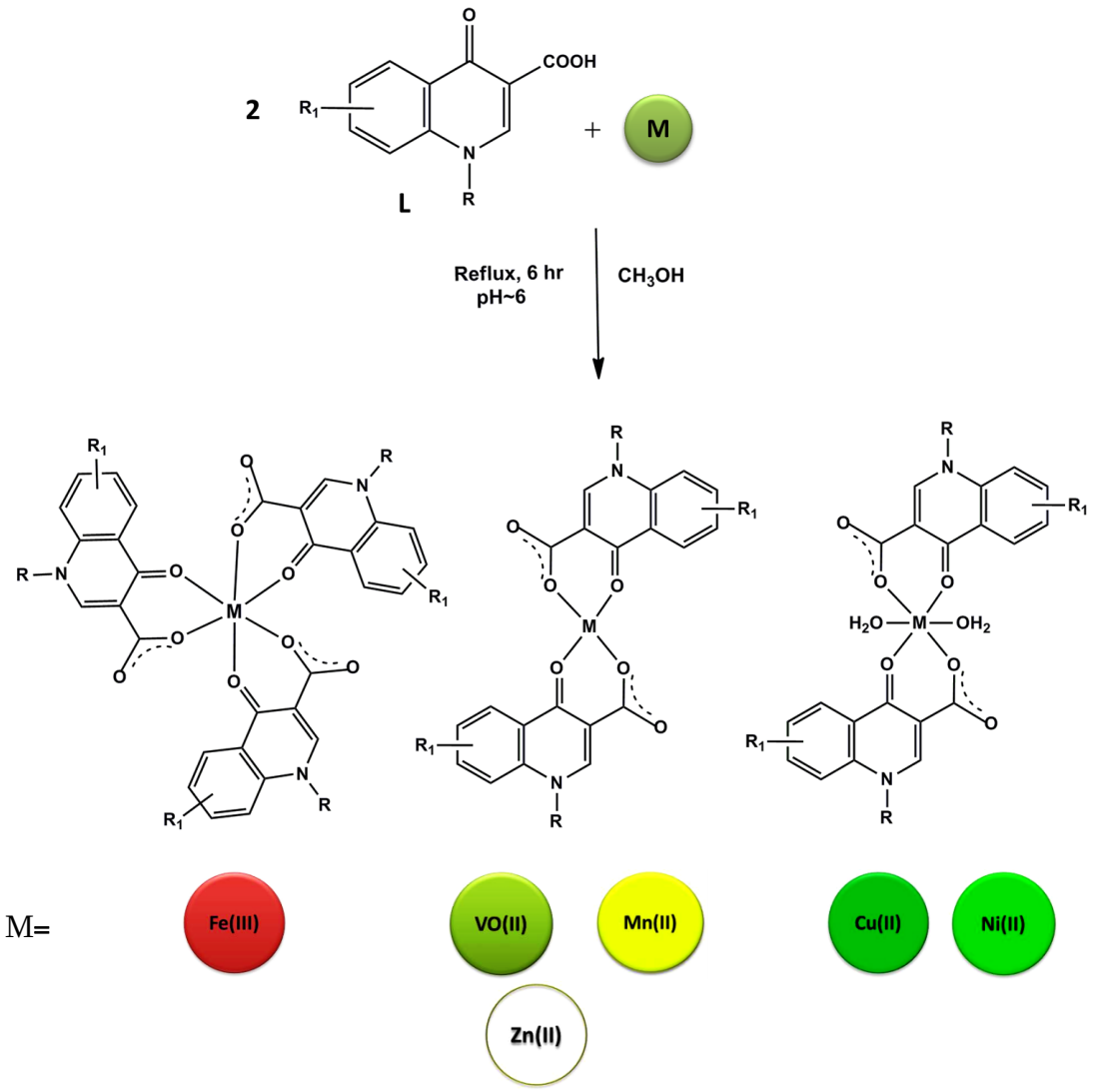

Scheme 3.1. General scheme for synthesis of metal fluoroquinolone complex.

3.3 Physicochemical data of the synthesized complexes

All the complexes were synthesized by the method described in section 3.2.

A. $[Fe(MFL)_3]$ (**1**)

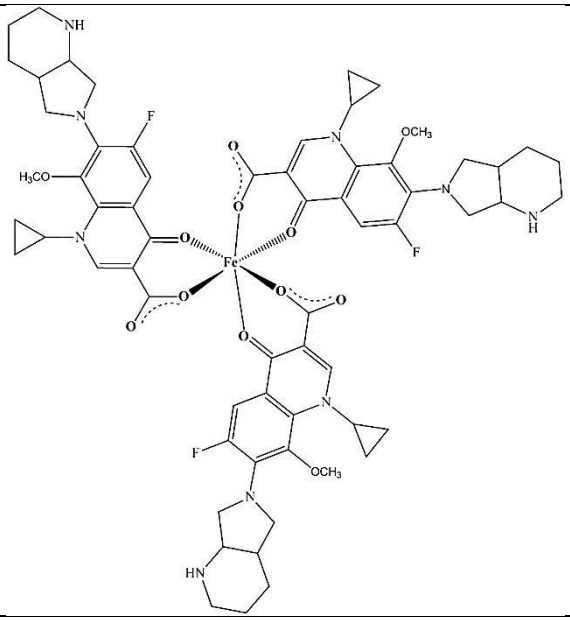

Yield: 72%
Molecular weight: 1260 g/mol
Molecular formula: $C_{63}H_{72}F_3N_9O_{12}Fe$
Calc. (%): C, 60.8; H, 5.8; N, 10.1; Fe, 4.4
Found (%): C, 61.0; H, 5.8; N, 10.1; Fe, 4.5
λ_{max}: 289, 333, 425, 610 nm.
ESI-MS [MeOH, *m/z*]: 1259.0 [M-1]
IR: 1583 (COO_{asym}), 1381(COO_{sym}), 1632 $(C=O)_{ketone}$

B. $[VO(MFL)_2]$ (**2**)

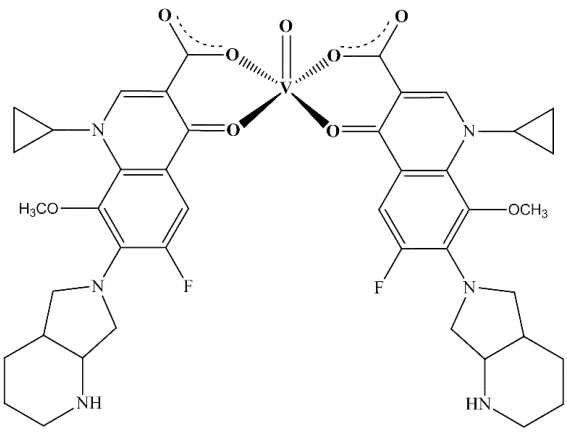

Yield: 68%,
Molecular weight: 869.80 g/mol
Molecular formula: $C_{42}H_{48}F_2N_6O_9V$
Calc. (%): C, 58.0; H, 5.56; N, 9.66; V, 5.86
Found (%): C, 58.5; H, 5.6; N, 9.9; V, 8.9
λ_{max}: 291, 339, 408, 675, 780 nm.
ESI-MS [MeOH, *m/z*]: 867.4 [M-2]
IR: 1578 (COO_{asym}), 1377(COO_{sym}), 1631 $(C=O)_{ketone}$

C. $[Cu(MFL)_2(H_2O)_2]$ (**3**)

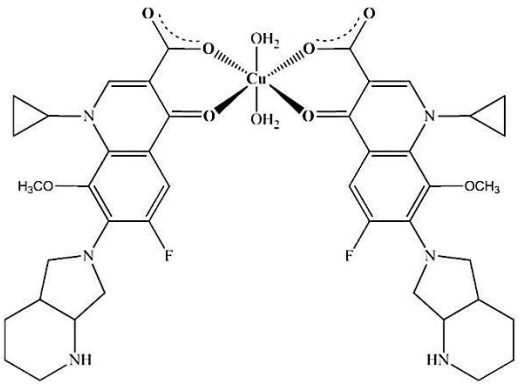	Yield: 65%, Molecular weight: 901.80 g/mol Molecular formula: $C_{42}H_{52}F_2N_6O_{10}Cu$ Calc. (%): C, 55.9; H, 5.8; N, 9.3; Cu, 7 Found (%): C, 56.0; H, 5.7; N, 9.4; Cu,7.5 λ_{max}: 288, 338, 405, 539 nm. ESI-MS [MeOH, *m/z*]: 900.1 [M-1] IR: 1580 (COO_{asym}), 1370(COO_{sym}), 1627 $(C=O)_{ketone}$

D. $[Ni(MFL)_2(H_2O)_2]$ (**4**)

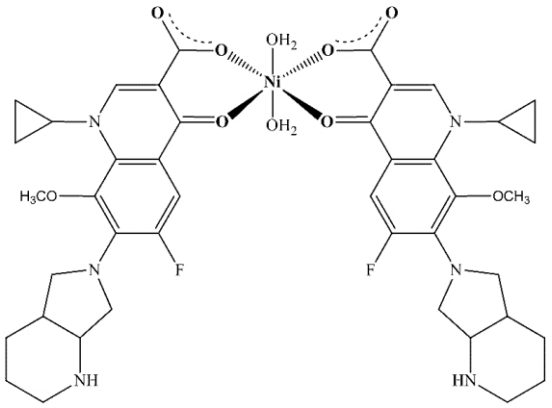	Yield: 63%, Molecular weight: 896.3 g/mol Molecular formula: $C_{42}H_{52}F_2N_6O_{10}Ni$ Calc. (%): C, 56.2; H, 5.8; N, 9.3; Ni, 6.5 Found (%): C, 56.3; H, 5.7; N, 9.3; Ni,6.7 λ_{max}: 287, 338. 403, 558, 681 nm, ESI-MS [MeOH, *m/z*]: 896.0 [M^+] IR: 1584 (COO_{asym}), 1383(COO_{sym}), 1633 $(C=O)_{ketone}$

E. $[Mn(MFL)_2]$ (**5**)

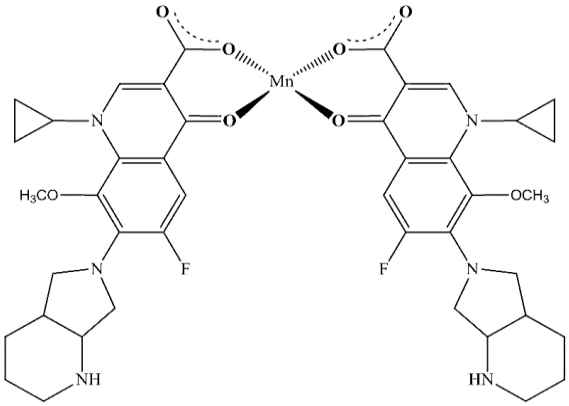	Yield: 69%, Molecular weight: 857.3 g/mol Molecular formula: $C_{42}H_{48}F_2N_6O_8Mn$ Calc. (%): C, 58.5; H, 5.6; N, 9.8; Mn, 6.4 Found (%): C, 56.7; H, 5.68; N, 9.5; Mn, 6.5 λ_{max}:287, 338, 403, 558, 681 nm. ESI-MS [MeOH, *m/z*]: 857.0 [M^+] IR: 1588 (COO_{asym}), 1382(COO_{sym}), 1629 $(C=O)_{ketone}$

F. [Fe(LFL)$_3$] (**6**)

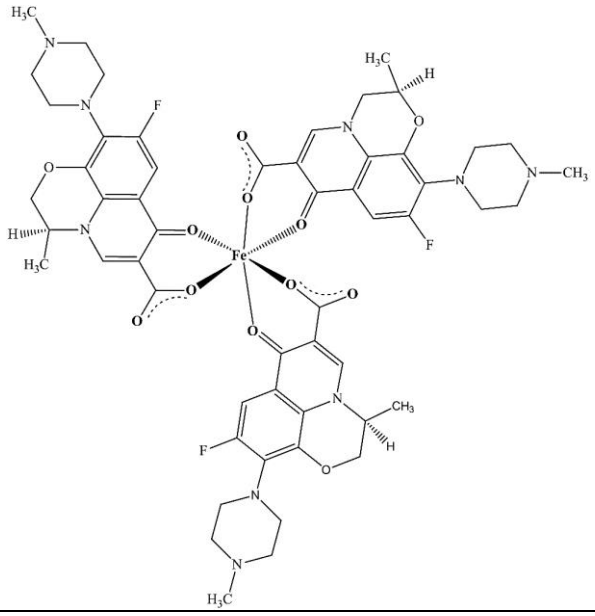	Yield: 82% Molecular weight: 1139 g/mol Molecular formula: $C_{54}H_{60}F_3N_9O_{12}Fe$ Calc. (%): C, 56.9; H, 5.31; N, 11.0; Fe, 4.9 Found (%): C,57.0; H, 5.34; N, 10.9; Fe, 4.9 λ_{max}: 290, 333, 404, 653 nm. ESI-MS[MeOH, *m/z*]: 1143.0 [M+4] IR: 1572 (COO_{asym}), 1333(COO_{sym}),1628 $(C=O)_{ketone}$

G. [VO(LFL)$_2$] (**7**)

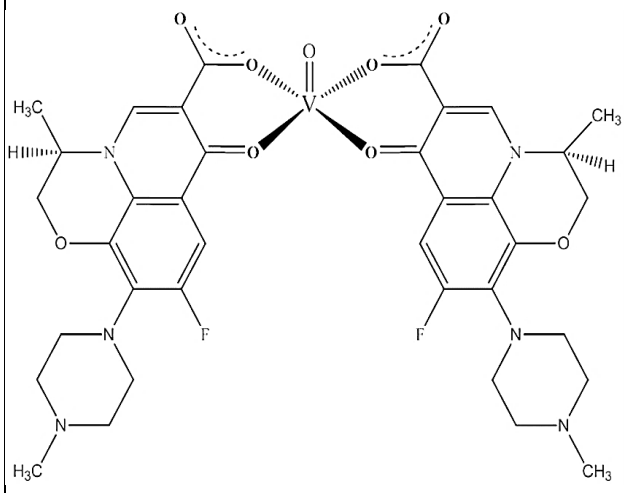	Yield: 71%, Molecular weight: 786.68g/mol Molecular formula: $C_{36}H_{40}F_2N_6O_9V$ Calc. (%): C, 54.7; H, 5.11; N, 10.64; V, 6.45 Found (%): C, 55.0; H, 5.0; N, 10.6; V, 6.42 λ_{max}:286, 332, 406, 605, 790 nm, ESI-MS [MeOH, *m/z*]: 787.6 [M+1] IR: 1588 (COO_{asym}), 1362(COO_{sym}),16232 $(C=O)_{ketone}$

H. $[Cu(LFL)_2(H_2O)_2]$ (**8**)

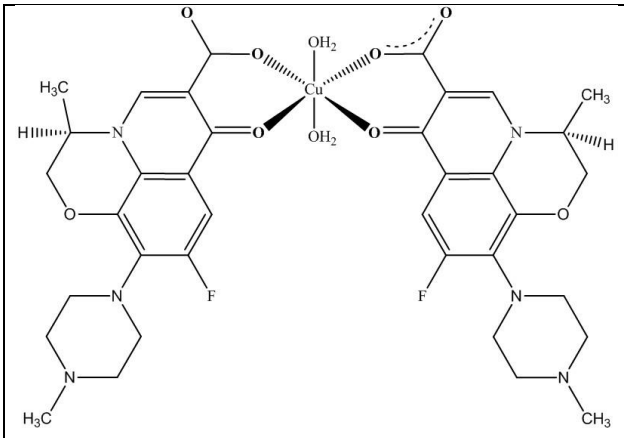

Yield: 69%,
Molecular weight: 821.80 g/mol
Molecular formula: $C_{36}H_{42}F_{20}N_6O_{10}Cu$
Calc. (%): C, 51.4; H, 5.04; N, 10.1; Cu, 7.57
Found (%): C, 52.0; H, 5.1; N, 10.0; Cu, 7.50
λ_{max}: 290, 330, 403, 635 nm,
ESI-MS [MeOH, *m/z*]:821 [M^+]
IR: 1584 (COO_{asym}), 1350 (COO_{sym}),1634 $(C=O)_{ketone}$

I. $[Ni(LFL)_2(H_2O)_2]$ (**9**)

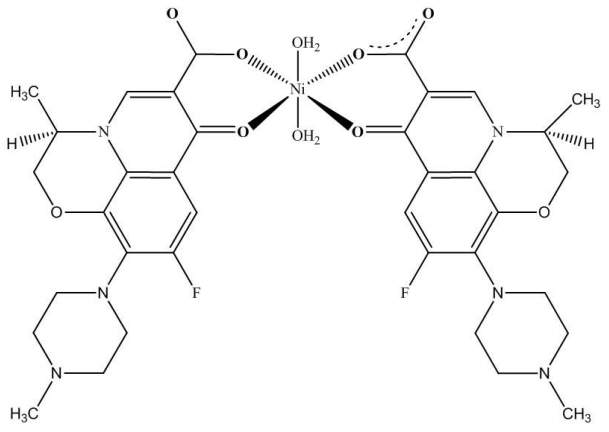

Yield: 64%,
Molecular weight: 816.3 g/mol
Molecular formula: $C_{36}H_{44}F_2N_6O_{10}Ni$
Calc.(%): C, 52.8; H, 5.4; N, 10.20; Ni, 7.1
Found (%): C, 53.3; H, 5.4; N, 10.29; Ni, 7.70
λ_{max}: 288, 331, 420, 535, 823 nm,
ESI-MS [MeOH, *m/z*]: 816 [M^+]
IR: 1568 (COO_{asym}), 1352 (COO_{sym}),1623 $(C=O)_{ketone}$

J. $[Zn(LFL)_2]$ (**10**)

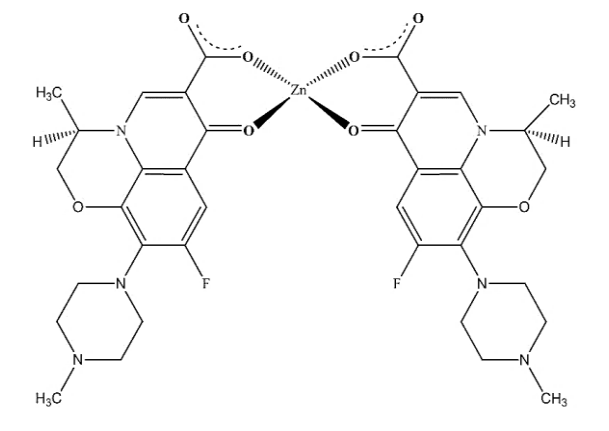

Yield: 78%,
Molecular weight: 785.5 g/mol
Molecular formula: $C_{36}H_{40}F_2N_6O_8Zn$
Calc.(%): C,54.5; H, 5.1; N, 10.6; Zn, 8.3
Found(%): C,55.0; H, 5.1; N, 10.0; Zn, 8.29
λ_{max}: 289, 334, 404nm.
ESI-MS [MeOH, *m/z*]: 783.0 [M-2]
IR: 1519 (COO_{asym}), 1388 (COO_{sym}),1634 $(C=O)_{ketone}$

3.4 Results and discussions

3.4.1 Synthesis and general properties

The metal complexes (**1-10**) were prepared in high yields (~70%) by the reaction of MFL and LFL with the metal chlorides in the ratio 3:1 for Fe(III) and 2:1 for all other metal (II) ions. The complexes are characterized by various spectroscopic and analytical techniques. All the complexes displayed the expected molecular ion peaks in their ESI-MS spectrum.

The IR spectra of the free ligands and their metal complexes were recorded in 4000-400 cm^{-1} range (Fig 3.1). The IR spectra of metal complexes were interpreted by comparing with the free ligands, in order to characterise their structures and mode of coordination of the ligands with the metal ions; the findings are listed in Table 3.1.

In the IR spectra of MFL and LFL the band observed at 1624 and 1628 cm^{-1} respectively is assigned to ν_{coo} stretching vibration . On coordination with the metal ions this band of free MFL/LFL has been replaced by two strong bands in the range 1519-1688$cm^{-1}$and 1333-1388cm^{-1} corresponding to $\nu_{coo(asym)}$ and $\nu_{coo(sym)}$ respectively. The difference $\Delta = [\nu_{asym}(CO_2) - \nu_{sym}(CO_2)]$ is a useful characteristic for determining the carboxylate coordination mode of the quinolone ligands. The Δ values for complexes (**1**–**10**) fall in the 201–239 cm^{-1} range indicating a monodentate coordination mode of the carboxylato group [14] of the MFL and LFL ligands. The pyridone stretch $\nu_{(c=o)p}$ is shifted from 1708 cm^{-1}(MFL) and 1712 cm^{-1} (LFL) to 1623-1634 cm^{-1} in the complexes; this shift in the band towards lower energy suggest coordination through pyridone oxygen atom. The overall changes in the IR spectra suggest that the MFL and LFL ligands are coordinated to metal ions *via* the pyridone and one carboxylate oxygen.

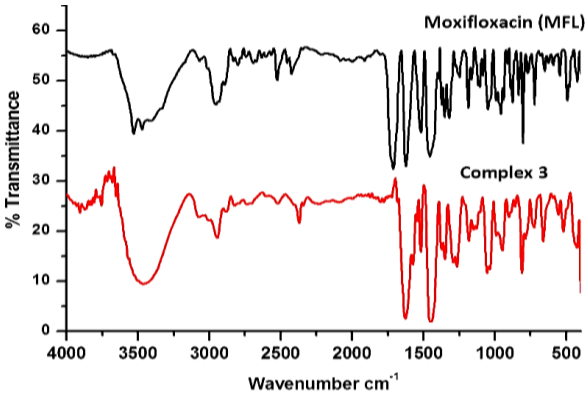

Fig 3.1: IR spectra of MFL and Complex **3**

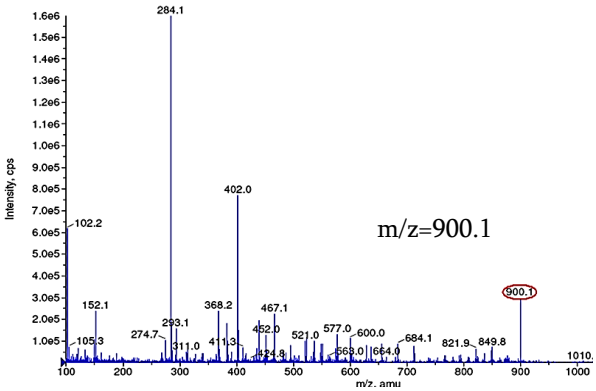

Fig 3.2: ESI-MS spectra of Complex **3**

Table 3.1: Characteristic IR bands (4000–400 cm^{-1}) of LFL and MFL complexes.

Compound	$\nu_{(C=O)p}$	$\nu_{(C=O)carboxyl}$	$\nu_{(COO)asym}$	$\nu_{(COO)sym}$	Δ	$\nu_{(M-O)}$
MFL	1708	1624	-	-	-	-
Complex 1	1632	-	1583	1381	202	-
Complex 2	1631	-	1578	1377	201	938
Complex 3	1627	-	1580	1370	210	538
Complex 4	1633	-	1584	1383	201	-
Complex 5	1629	-	1588	1382	206	-
LFL	1712	1628	-	-	-	-
Complex 6	1628	-	1572	1333	239	-
Complex 7	1632	-	1588	1362	226	924
Complex 8	1634	-	1584	1350	234	536
Complex 9	1623	-	1568	1352	216	-
Complex 10	1634	-	1519	1388	231	-

The UV–Vis spectra of the ligands and metal complexes **1-10** were recorded in aqueous solution. The MFL ligand showed characteristic intra ligand bands at 285 and 338 nm, whereas for LFL the bands were observed at 286 and 331nm. However, the peaks shifted in the range of 287-290 nm and 330-340 nm respectively on coordination with the metal ions. All the complexes exhibited an absorption bands at 400-425 nm which was assigned to the ligand-to-metal charge-transfer transition in addition to the weak absorption bands in the visible region, characteristic of d-d transitions whose positions and assignments are summarized in table 3.2.

Table 3.2: Electronic spectral data of complexes **1-10.**

Compound	Intra ligand charge transfer bands (π-π^*)		Charge transfer bands (LMCT)	d-d transitions	
MFL	285	338			
LFL	286	331			
Complex 1	289	333	425	610	$^6A_{1g} \rightarrow {}^4T_{1g}$
Complex 2	291	339	408	639(band I) 780(band II)	$b_2(d_{xy}) \rightarrow b_1(d_{x^2-y^2})$ $b_2(d_{xy}) \rightarrow e(d_{xz}; d_{yz})$
Complex 3	288	338	403	539	$2E_g \rightarrow 2T_{2g}$
Complex 4	287	338	403	558 (band I) 681(band II)	$^3A_{2g} \rightarrow {}^3T_{1g}$ (P) $^3A_{2g} \rightarrow {}^3T_{1g}$ (F)
Complex 5	287	340	402	-	-
Complex 6	290	333	404	653	$^6A_{1g} \rightarrow {}^4T_{1g}$
Complex 7	287	340	402	605(band I) 780(band II)	$b_2(d_{xy}) \rightarrow b_1(d_{x^2-y^2})$ $b_2(d_{xy}) \rightarrow e(d_{xz}; d_{yz})$
Complex 8	290	330	403	635	$2E_g \rightarrow 2T_{2g}$
Complex 9	288	331	420	535 (band I) 823(band II)	$^3A_{2g} \rightarrow {}^3T_{1g}$ (P) $^3A_{2g} \rightarrow {}^3T_{1g}$ (F)
Complex 10	289	334	404	-	-

The EPR spectra of copper and vanadyl complexes exhibited good hyperfine splitting (Fig. 3.3) and the corresponding $g_{\|}$, $g_{\perp}$ and $A_{\|}$ values are tabulated in Table 3.3. The low temperature X-band EPR spectra of complex **3** and **8** at 10 K in dmso were typical for

mononuclear Cu^{2+}complexes in a distorted octahedral geometry [15]. A well resolved nuclear hyperfine splitting of $g_{\|}$ signal due to copper nuclei in parallel orientation is observed whereas no observable splitting of $g_{\perp}$ signal is seen. The values $g_{\|}>g_{\perp}>2.0023$ is typical of axially symmetric d^9 Cu(II) having one unpaired electron in $d_{x^2-y^2}$ orbital of the metal ion. In axial symmetry, the G-parameter defined as $G = g_{\|}-2/g_{\perp}-2$ reflects the spin interaction between Cu(II) centres in solid polycrystalline complexes. According to Hathaway [16] if G > 4, the spin–exchange interaction is negligible and if it is less than 4 considerable spin -exchange interaction prevails. In the present case the value of exchange interaction term G>4 (Table 3.3) indicates absence of Cu-Cu interaction, thus supporting proposed monomeric structure.

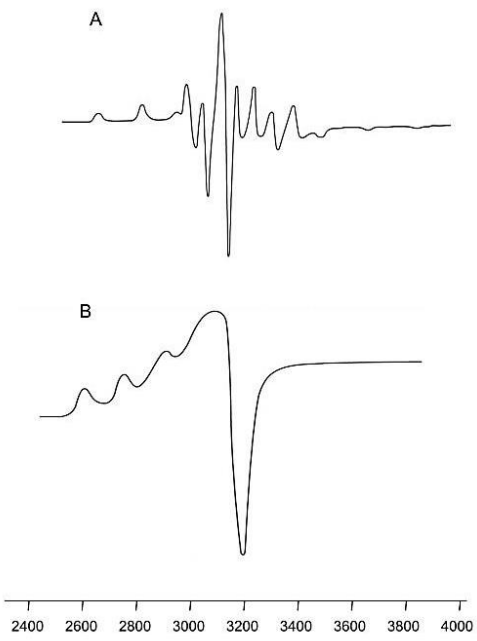

Fig 3.3: ESR spectra of (A) complex **2** & (B) complex **3** in DMSO. EPR conditions: Temp, 10K; microwave power, 5.0 mW; Modulation amplitude, 1G; microwave frequency, 9.1 Ghz

Table 3.3: X-band ESR parameters of complex **2**, **3**, **7** and **8**.

Compound	$g_{\|}$	$g_{\perp}$	$g_{average}$	$A_{\|}$	G	α^2
Complex 2	2.04	1.90	1.95	171×10^{-4}	4.3	0.06
Complex 3	2.27	2.06	2.129	156×10^{-4}	4.5	0.72
Complex 7	2.11	2.01	2.18	185×10^{-4}	5.3	0.056
Complex 8	2.27	2.06	2.13	150×10^{-4}	4.6	0.68

The EPR spectra of complexes **2** and **7** were typical for a mononuclear VO^{2+} complexes. The parameters $g_{\|}$ and $A_{\|}$ have been estimated by considering the position of the outermost lines and the experimentally deduced pair of their values supports an O_4 basal plane. The value of $A_{\|}$ is helpful in predicting the donor atoms at the equatorial sites of the VO^{2+}moiety through the "additivity principle" [17]. In the present case, the donors involved are two $O_{carboxyl\ and}$ two O_{ketone} atoms of MFL/LFL ligands.

Thermo-gravimetric analyses of the complexes were carried out at 10°C per min in a temperature range 50°C - 850°C in N_2 atmosphere (Fig 3.4). The complexes **3, 4, 8** and **9** show a weight loss in the range 100°C–200°C corresponding to the decomposition of coordinated water molecules. Beside this, the weight loss corresponding to the ligands (MFL/LFL) occurred in a single step between 200 to 850 °C for all the complexes, leaving behind the metal oxide residue.

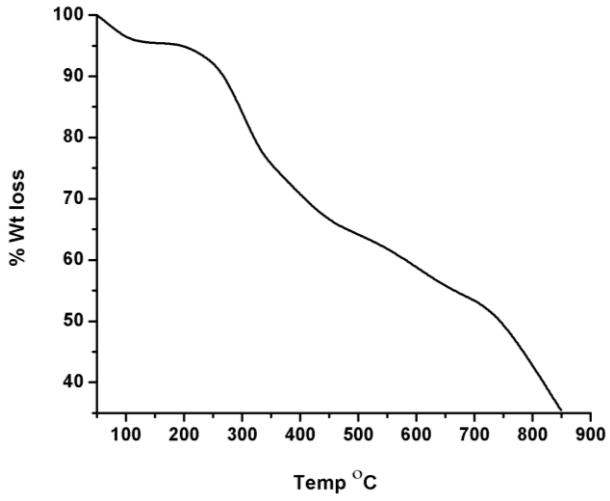

Fig 3.4: Thermal degradation curve of the complex **3** at heating rate of 10 °C per minute under N_2 atmosphere.

3.4.1.2 Electrochemical Studies

Redox behavior of the moxifloxinato complexes (**1-5**) have been investigated by cyclic voltammetry in DMSO using 0.1M Tetraethylammonium perchlorate (TEAP) as supporting electrolyte. The representative cyclic voltammetry profile of complex **3** is given in Fig. 3.5 and the electrochemical data of the complexes are presented in Table 3.4.

In dmso solution, complete scan of **1** in the range 0.0 V to -1.2 V shows a cathodic wave at -0.840 V and an anodic wave at -0.652 V assigned to the couple Fe (III) / Fe (II). The ΔE value is greater than the Nernstian value (0.059V) for a one-electron reduction. This indicates a considerable reorganization of the coordination sphere during electron transfer. **2** exhibits a cathodic wave at -0.980 V and an anodic wave at -0.700 V in dmso attributed to the couple V(IV)/V(III). The complete scan in the range +0.8 V to -0.6 V for **3** (Fig. 3.5) in dmso shows a broad cathodic wave at ~ -0.285 V assigned to the reduction process $Cu^{II} \rightarrow Cu^{I}$. In the reverse scan an anodic wave at + 0.135 V assigned to the oxidation process $Cu^{I} \rightarrow Cu^{II}$ was observed. The facile interconversions of the Cu^{2+}/Cu^{1+} may have relevance to the biological activities of the compound, since intracellular accumulation of Cu^{1+} moieties even in slight excess have been known to generate oxidative stress which is detrimental to cancer cells. Complex **4** in dmso solution exhibits a cathodic wave at -1.180 V and an anodic wave at -0.690 V in the scan range +1.2 V to -1.2 V representing the couple

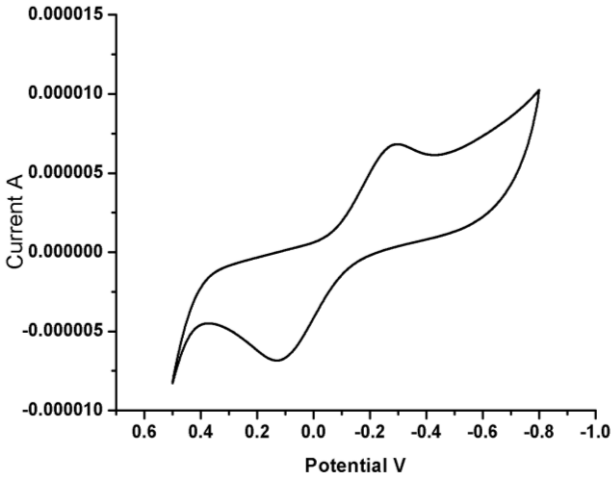

Fig 3.5: Cyclic voltammograms of 0.4 mM dmso solution of **3**. (Supporting electrolyte = TEAP, 0.1 M). Scan rate = 100 mV s^{-1}.

Ni(II)/Ni(I). The cathodic and anodic waves corresponding to the couple Mn(II)/Mn(I) are observed at -0.939 V and -0.711 V respectively for **5** in dmso solution.

Table 3.4 : Redox couples of the complexes **1-5**, their cathodic and anodic potentials.

Compounds	Redox couple	Epc(V)	Epa(V)	ΔEp(V)
Complex 1	Fe(III)/Fe(II)	-0.840	-0.652	0.188
Complex 2	$V^{(IV)}/V^{(III)}$	-0.980	-0.700	0.280
Complex 3	$Cu^{(II)}/Cu^{(I)}$	-0.285	+0.135	0.150
Complex 4	Ni(II)/Ni(I)	-1.180	-0.690	0.490
Complex 5	Mn(II)/Mn(I)	-0.939	-0.711	0.228

3.4.2 Antimicrobial Activity

The complexes were screened for their *in vitro* anti-microbial activity against gram positive and gram negative bacteria by using disc agar diffusion method [17] with concentrations 5, 10, 25, 50 and 100μg/mL. The zone of inhibition values indicate that most of the complexes have higher anti-microbial activity compared to the free ligands (MFL/LFL) (Table 3.5). The higher anti-microbial activity of the metal complexes compared to the free quinolone drugs can be explained on the basis of chelation theory [18]. Chelation considerably reduces the polarity of the metal ion because of partial sharing of its positive charge with donor groups and possible electron delocalization over the whole chelate ring. In addition chelation could enhance the lipophilic character of the central metal atom, which subsequently favours its permeation through the lipid layer of the cell membrane.

Table 3.5: Zone of inhibition of MFL/LFL and their complexes **1-10** (1 μg/μL)

Compound	Gram (+ve)		Gram (-ve)	
	S. aureus	*B. subtilis*	*P. aeruginosa*	*E. coli*
MFL	11	14	12	09
Complex 1	15	16	16	16
Complex 2	15	18	14	15
Complex 3	19	22	16	21
Complex 4	16	20	13	18
Complex 5	17	17	15	19
LFL	16	18	14	11
Complex 6	14	20	18	14
Complex 7	16	22	17	16
Complex 8	21	28	20	18
Complex 9	15	19	19	15
Complex 10	19	20	16	13

3.4.3 DNA binding studies

Efficient nuclease activity requires efficient DNA binding propensity of the synthetic nucleases. The metal complexes can bind to DNA via covalent (a labile ligand is replaced with a nitrogen atom of DNA base, such as guanine N7) or noncovalent interactions. Noncovalent binding of small molecules to DNA can be reversible and is usually categorized by three major types groove binding, intercalation and metalloinsertion as shown in Fig. 6. [19]

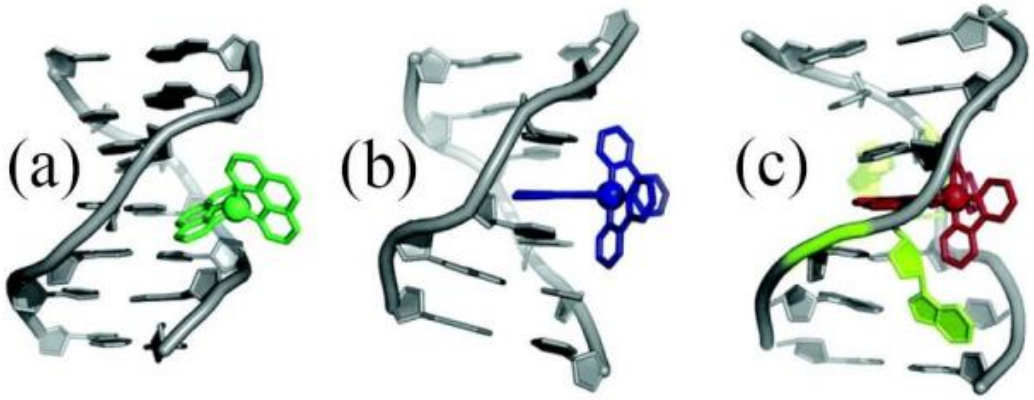

Fig 3.6: Different noncovalent binding modes of metal complexes with DNA: (a) groove binding (b) intercalation, and (c) metalloinsertion

There are different methods by which one can determine the mode and the strength of binding of a metal complex to duplex DNA. This includes: (i) fluorescence intensity quenching method which uses the principle of quenching in the emission intensity of fluorescing molecules viz. DNA-EB (EB=ethidium bromide); (ii) electronic spectroscopy can be used by observing the hypochromism/hyperchromism and bathochromic/hysochromic shift of the absorption bands of the metal complexes or DNA; (iii) viscosity measurement giving information related to intercalative or groove (minor/major) binding mode; (iv) electrochemistry, by measuring the decrease in current height to get the extent of binding and change in potential to get mode of binding (v) circular dichroism spectroscopic technique for the information about

conformational changes of DNA. We have used all the above stated techniques for studying the binding properties of the complexes.

3.4.3.1 UV-Visible absorption titration

Study of the interaction of quinolones and their complexes with DNA is important since their activity as antibacterial and anticancer drugs is focused on the inhibition of DNA replication by targeting essential type II topoisomerases. UV spectroscopic titration is an effective method to examine the mode of binding of metal complexes to DNA [20] since the observed changes in the spectra of complexes/DNA may give evidence of the existing interaction and its mode [21].

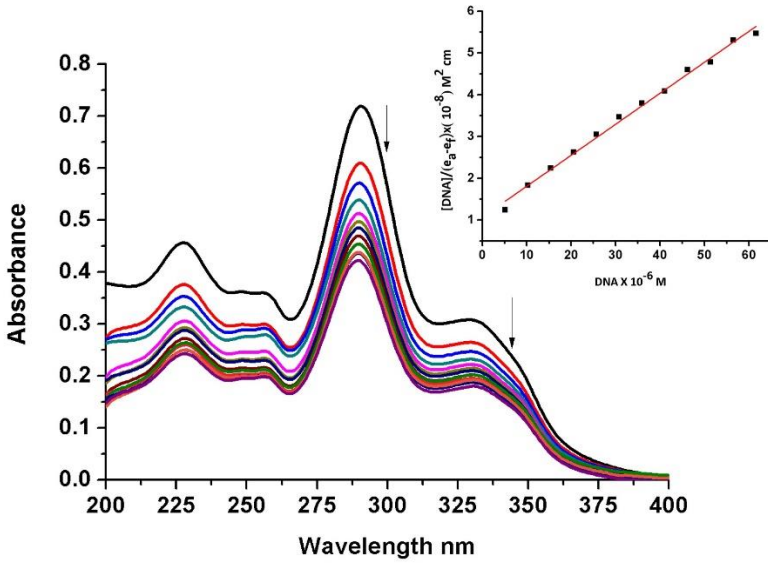

Fig 3.7: Absorption spectra of **3** (5μM) showing the decrease in absorption intensity on gradual addition of CT-DNA(0-35 μM) in 5 mM Tris-HCl buffer (pH, 7.2) at 25°C. Inset shows the plot of [DNA]/(ε_A-ε_f) vs [DNA].

In general, hyperchromism and hypochromism are the spectral features of DNA concerning changes of its double helix structure; hyperchromism indicates the breakage of the secondary structure of DNA and hypochromism reveals binding of complex to DNA via intercalation. A complex bound to DNA through intercalation generally causes hypochromism and red shift (bathochromism) of the absorption bands due to strong stacking interaction between the aromatic chromophore of the complex and the base pairs of DNA [22]. The π* orbital of the intercalated ligand can couple with the π orbital of the base pairs, thus reducing the π–π* transition energy and

resulting in bathochromism. If the coupling orbital is partially filled by electrons, it results in a decrease of the transition probabilities and concurrently results in hypochromism. We have used the absorption spectral technique to determine the intrinsic binding constant and the binding mode to CT DNA by monitoring the absorption intensity of the spectral band at 289 nm with increasing concentration of CT-DNA keeping the complex concentration constant. The present complexes show hypochromism (decrease in the intensity of the intra ligand band upon addition of increasing amounts of CT-DNA) and red shift (~2-3 nm) indicating intercalative nature of binding (Fig 3.7). The changes in the absorbance at λ_{max} of the complexes with the increasing concentration of CT-DNA was used to calculate the intrinsic binding constant, K_b using equation 2.1 [22].

$$[DNA]/(\varepsilon a - \varepsilon f) = [DNA]/(\varepsilon b - \varepsilon f) + 1/K_b\,(\varepsilon b - \varepsilon f)$$

Where [DNA] is the concentration of DNA in base pairs, εf correspond to the extinction coefficient of the free metal complex (**1-10**), and εb is the extinction coefficient of the metal complex in the fully bound form. The binding constants (K_b) of the metal complexes with DNA were obtained from the ratio of slope to intercept by using the plot of [DNA]/(εa– εf) versus [DNA] (Fig 3.7. Inset). The binding constant (K_b) (Table 3.6) are in the order of 10^6 M^{-1} and are higher than that of free ligands (MFL/LFL), suggesting that the binding affinity of the fluoroquinolone drugs to CT DNA is enhanced on coordination to transition metals.

3.4.3.2 Fluorescence quenching Studies

The finding of hypochromism and bathochromism in spectroscopic studies for the binding of metal complexes can be taken as an evidence for intercalation, but such data alone are insufficient to rule out alternative binding mechanisms. Therefore, the

binding of the complexes to DNA have been studied by competitive fluorescence quenching experiments. In general, when small molecules bind to DNA, changes in fluorescence is noted in the emission spectrum relative to what is observed in DNA. Ethidium bromide (EB = 3,8-diamino-5-ethyl-6-phenylphenanthridinium bromide) does not show any appreciable emission in buffer solution due to fluorescence quenching by solvent molecules. However EB emits intense fluorescence in the presence of CT DNA as a result of strong intercalation of the planar phenanthridine ring between adjacent base pairs on the double helix; therefore, EB is considered a typical indicator of intercalation [24]. The changes observed in the fluorescence emission spectrum of a solution containing EB bound to DNA may be used to study the interaction between DNA and other compounds, such as metal complexes, since the addition of a compound, capable to intercalate to DNA equally or more strongly than EB, could result in a quenching of the EB–DNA fluorescence emission [25].

The emission spectra of EB bound to CT DNA in the absence and presence of each complex have been recorded for [EB] = 20μM, [DNA] = 26μM and increasing amounts of the complex. The addition of complexes **1–10** at diverse r ([compound]/[DNA]) values results in a moderate decrease in the intensity of the emission band (Fig. 3.8(a)) of the DNA–EB system at 610 nm (the final fluorescence is up to 33–49% of the initial EB–DNA fluorescence intensity for all complexes, Fig. 3.8(b)) indicating the existence of a competition between complexes and EB in binding to DNA. The observed quenching of DNA–EB fluorescence by the complexes suggests that they displace EB from the DNA–EB adduct, thus probably interacting with CT DNA by the intercalative mode [26].

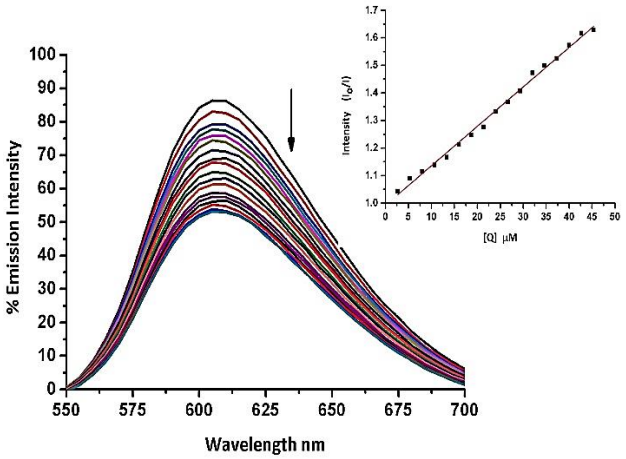

Fig 3.8: (a) The emission spectra of DNA bound EB in the presence of increasing concentration of complex **3** (0 -100 µM). DNA=26µM.
Inset: Stern volmer plot Io/I vs Q (concentration).

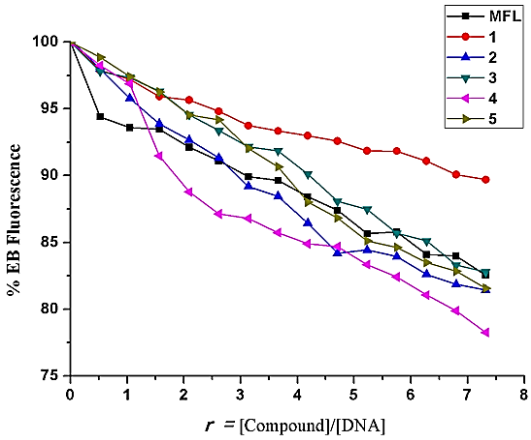

Fig 3.8: (b) Plot of DNA-EB relative Fluorescence intensity (% I/Io) vs *r at* λ_{em}= 610 nm in the presence of **1–5**. (*r*=[compound]/[DNA]) in buffer solution) at pH 7.0).

The relative binding of complexes to CT-DNA was determined by calculating the quenching constant (K_{SV}) from the slopes of straight lines obtained from the Stern-Volmer equation (2.2):

$$Io/I = 1 + K_{SV}[Q]$$

where Io and I are the emission intensities in the absence and the presence of the quencher (**1-10**) respectively, [Q] is the concentration of the quencher and K_{SV} is the Stern–Volmer constant which can be obtained from the slope of the plot of Io/I *versus* [Q] and is often used to evaluate the quenching efficiency of each compound. The Stern–Volmer plots of EB–DNA in the presence of **1-10** illustrate that the quenching of EB bound to DNA by the compounds is in good agreement (R = 0.99) with the linear Stern–Volmer equation (Eq. (2.2)) [26]. The values (Table 3.6) of the Stern–Volmer constants (K_{SV}) obtained show that the complexes can bind tightly to DNA, with the binding constant ranging between 2.6-9.4 x 10^6 M^{-1}.

Table 3.6: DNA binding constants (K_b) and Stern–Volmer quenching constants (K_{SV}) of complexes **1–10**.

Compound	K_b	% Hypo-chromism	Red shift nm	Ksv	% decrease in emission intensity of DNA-EB
MFL	1.0×10^5	9%	-	2.6×10^5	12%
Complex 1	3.1×10^6	15%	2	6.5×10^6	28%
Complex 2	2.1×10^6	20%	3	2.9×10^6	32%
Complex 3	8.5×10^6	33%	3	5.8×10^6	49%
Complex 4	2.0×10^6	27.2%	2	2.8×10^6	30%
Complex 5	1.5×10^6	25%	2	2.6×10^6	34%
LFL	4.0×10^4	15%	-	4.0×10^5	16%
Complex 6	5.7×10^6	20%	3	8.2×10^6	38%
Complex 7	5.3×10^6	33%	3	6.5×10^6	32%
Complex 8	6.9×10^6	27%	2	9.4×10^6	46%
Complex 9	5.1×10^6	25%	2	6.0×10^6	35%
Complex 10	4.9×10^6	28%	2	5.9×10^6	27%

3.4.3.3 Viscometric titration

Viscosity measurements were carried out to further verify the interaction of the metal complexes with DNA. A hydrodynamic measurement such as viscosity is sensitive to length change and is regarded as the least ambiguous and most critical test of a binding model in absence of crystallographic data. Interaction of a foreign moiety to DNA which alters the length of DNA duplex is directly reflected on the intrinsic viscosity of DNA depending on the mode of interaction [27]. When the complexes interact with the DNA electrostatically, no effect on relative viscosity of DNA is observed because in this case the interaction between ligand and DNA occurs at minor groove which does not alter the native form of double helix.

In classical intercalation, the intercalating agents are expected to elongate the double helix to accommodate the ligand in between the bases, leading to an increase in the viscosity of DNA. In contrast, a partial or non-classical intercalation of the ligand could bend or kink the DNA helix, reduce its effective length and concomitantly the viscosity (Fig. 3(a)).

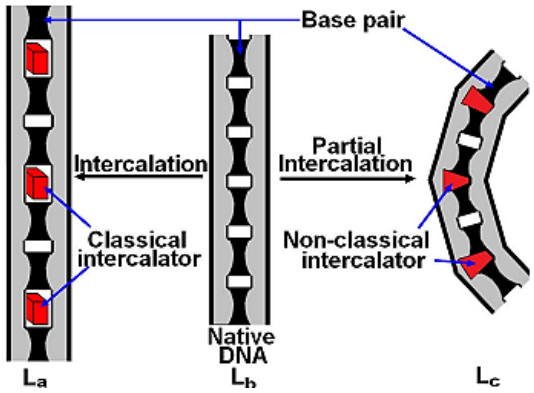

Fig 3 (a): Sketch representing the change in length (L) of DNA duplex (L_b) when ligand interacts via classical intercalation (L_a) and non–classical (partial) intercalation L_c); $L_a > L_b > L_c$

Since the relative specific viscosity (η/η_0) of DNA gives a measure on the increase in contour length associated with the separation of DNA base pairs due to intercalation, a DNA intercalator like ethidium bromide shows significant increase in the viscosity of the DNA solutions. η and η_0 are the specific viscosities of DNA in the presence and absence of the compounds, respectively) [28]. The plot of relative specific viscosity $(\eta/\eta_0)^{1/3}$ versus [complex]/[DNA] ratio (Fig. 3.9) for the complexes showed increase in the viscosity with the increase in the concentration of **1-10**, indicating intercalating nature of the complexes.

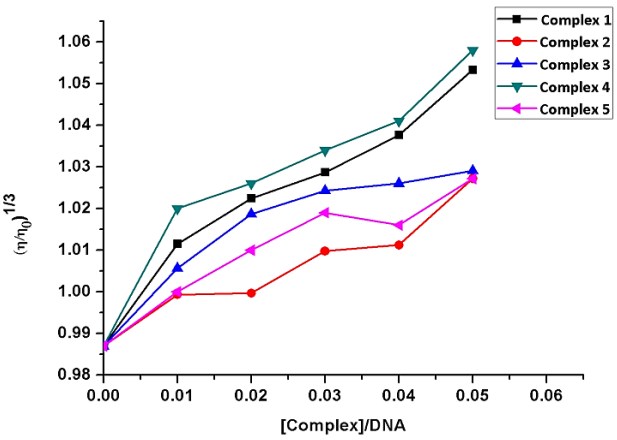

Fig 3.9 : The relative viscosity of DNA (50 μM) in the presence of complexes **1-5** (0 -60 μM) at 37.0 ºC in 5 mM Tris-HCl buffer (pH, 7.2).

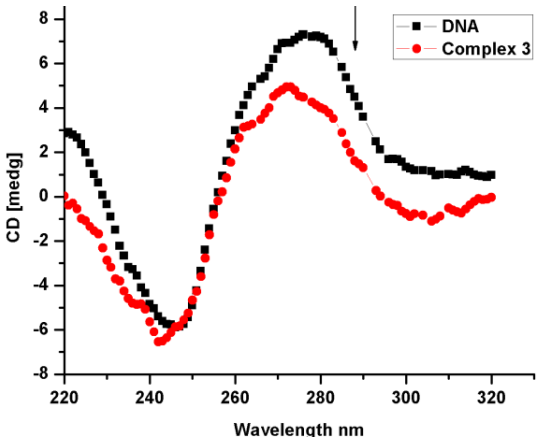

Fig 3.10: CD- Spectra of Calf-thymus DNA in 5 mM Tris-HCl buffer (pH, 7.2)in presence and absence of **3**. The spectra were recorded at 25°C after the samples had been incubated with CT-DNA for 10 min at 37°C.

3.4.3.4 Circular dichroism spectroscopy

The CD spectrum of free CT-DNA consists of a positive band at 275 nm and a negative band at 245 nm. CD spectroscopy is useful in diagnosing changes in the DNA conformation during drug-DNA interactions, as the positive band due to base stacking and negative band due to right handed helicity are quite sensitive to the mode of DNA interactions with small molecules [29]. Simple groove binding show little or no perturbation on the helicity, while intercalation enhances the intensities of both the bands by stabilizing the right handed B-conformation of CT-DNA [30]. In the presence of complexes **1-5,** there was a slight blue shift in both bands; furthermore, the intensity of the positive band decreased whereas that of the negative band increased (Fig. 3.10). These changes provided evidence for interaction between the complexes and DNA, but the exact nature of binding could not be identified.

3.4.3.5 Electrochemical studies

Electrochemical investigations of metal–DNA interactions can provide a useful supplement to spectroscopic methods and give information about interactions with both the reduced and oxidized forms of the metal complexes [31]. The electrochemical potential of a small molecule shifts positively when it intercalates into DNA double helix, while a negative shift of the potential is observed for an electrostatic interaction to DNA. Additionally, in the case of more potentials than one, a positive shift of Ep_1 and a negative shift of Ep_2 could imply that the molecule binds to DNA by both intercalation and electrostatic interaction. The quasireversible redox couples for complexes **1-5** have been studied upon addition of CT-DNA and the shifts in the cathodic (E_{pc}) and anodic (E_{pa}) potentials are given in Table 3.7. No new redox peaks appeared after addition of CT-DNA, but the current intensity of the peaks decreased, suggesting interaction of the complexes with CT-DNA. The cyclic voltammogram of a representative complex **3** in the presence of CT-DNA is shown in Fig. 3.11.

Complex **1** showed a positive shift for cathodic potential (E_{pc}) and a small negative shift for anodic potential (E_{pa}). **2** and **3** showed positive shifts for both E_{pc} and E_{pa}, whilst a positive shift in cathodic potential and no shift in anodic potential were observed for **4** and **5**. These shifts are consistent with binding of complexes

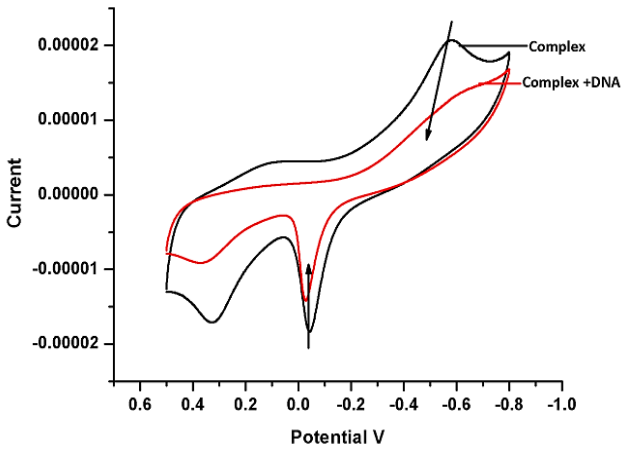

Fig 3.11: Cyclic voltammogram of 0.4 mM ½ dmso/buffer solution of **3** in the absence and presence of CT DNA. The arrows show the changes upon addition of CT DNA. Scan rate = 100 mV s^{-1}, supporting electrolyte = buffer solution.

1-5 to DNA by intercalation however the coexistence of electrostatic interaction in the case of **1** (negative shift of E_{pa}) cannot be ruled out [32].

Table 3.7: Redox couples of the complexes **1-5**, their cathodic and anodic potentials and the shift of the potentials in the absence and presence of CT-DNA.

Complex	Redox couple	Epc^f (mV)	Epc^b (mV)	ΔEpc (mV)	Epa^f (mV)	Epa^b (mV)	ΔEpa (mV)
1	$Fe^{(III)}/Fe^{(II)}$	-328	-314	+14	+204	+202	-2
2	$V^{(IV)}/V^{(III)}$	-838	-826	+12	-781	-753	+28
3	$Cu^{(II)}/Cu^{(I)}$	-580	-575	+5	-43	-28	+15
4	$Ni^{(II)}/Ni^{(I)}$	-287	-275	+12	-102	-102	0
5	$Mn^{(II)}/Mn^{(I)}$	-466	-439	+27	-280	-280	0

E_{pc}^f/ E_{pa}^f : cathodic/anodic potential of the free complex.
E_{pc}^b/ E_{pa}^b : cathodic/anodic potential of the complex bound to CT DNA.
$\Delta E_{pc} = E_{pc}^b - E_{pc}^f$.
$\Delta E_{pa} = E_{pa}^b - E_{pa}^f$.

3.4.4 Nuclease activity

DNA cleavage facilitated by transition metal complexes is the centre of interest. The extent of cleavage and transformation of native SC form of DNA (form I) to OC form (form II) and NC form (form III) under the influence of **1-10** were measured. When plasmid DNA was subjected to electrophoresis in the presence of the complexes, the fastest migration was observed for SC form, the slowest moving was OC form produced upon relaxing of SC form, the intermediate moving was NC form, generated upon cleavage of OC form. The results of DNA cleavage experiments for complexes **1-10** are shown in Fig. 3.12 (a) & (b). The results reveal that all the synthesized complexes show higher DNA cleavage ability compare to the drugs. Therefore it can be concluded that

DNA cleavage ability of the drugs (MFL/LFL) was enhanced on coordination with the metal ions.

Fig 3.12: a) Photogenic view of interaction of pUC19 DNA (150 μg/mL) with **1-5 (**200 μM) incubated for 6 hours at 37 °C: Lane 1, DNA control; Lane 2, **MFL**; Lane 3, DNA + **1**; Lane 4, DNA + **2**; Lane 5, DNA + **3**; Lane 6, DNA + **4**; Lane 7, DNA +**5**.

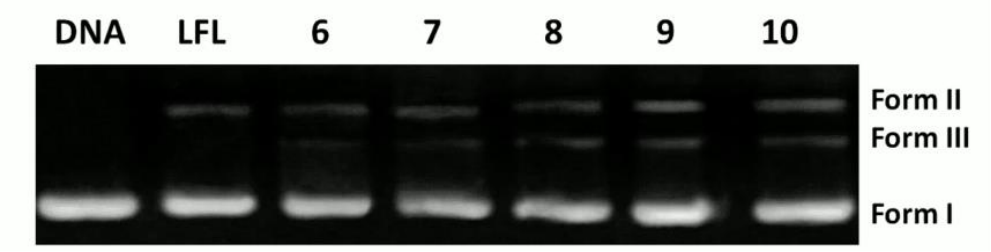

Fig 3.12: b) Photogenic view of interaction of pUC19 DNA (150 μg/mL) with **6-10 (**200 μM) based complexes incubated for 6 hours at 37 °C: Lane 1, DNA control; Lane 2, **MFL**; Lane 3, DNA + **6**; Lane 4, DNA +**7**; Lane 5, DNA + **8**; Lane 6, DNA + **9**; Lane 7, DNA +**10**.

3.4.5 Interaction with Proteins

Upon entry into the blood circulation, most drugs bind to plasma proteins and/or other blood components (eg. red blood cells). It is generally accepted that only the free drug molecules can arrive at the site of action that may be enzymes or receptors, and at steady state drug effect are directly proportional to the free concentration in plasma. Free drugs are rapidly distributed into tissues, resulting in direct binding to tissue proteins. Only free drug molecules can get across cellular membrane via passive diffusion or active mechanisms by various drug transporters. Therefore, the binding of drugs to plasma and tissue proteins is common and is considered to be an important factor determining the pharmacokinetics and pharmaco dynamics of drugs.

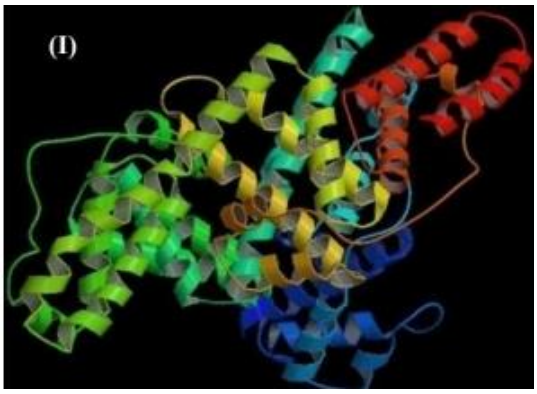

Fig 3(b): Structure of bovine serum albumin

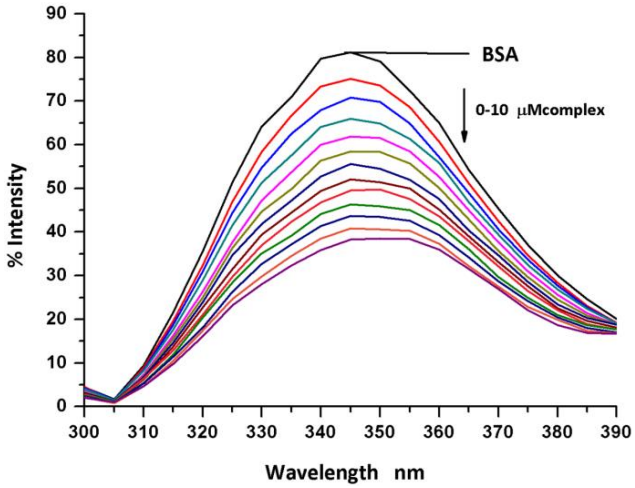

Fig 3.13: Emission spectra of BSA (6.6 μM) in presence of complex 8(0-10 μM) in tris buffer at 37˚C.

Most drugs bind to proteins in a reversible manner by means of weak chemical bonds such as ionic, van der Waals, hydrogen & hydrophobic bonds with the hydroxyl, carboxyl or other reversible sites available in the amino acids that constitute the protein chain. Within the plasma proteins, serum albumin is undoubtedly the most important carrier for drugs and other small molecules. The information about the number of binding

sites, the binding constants, the location of the sites, the binding forces etc. provides useful insight about the significance of the plasma protein binding for distribution and pharmacological activity of the drugs. Hence, understanding the drug-protein interactions is important in pharmacology, drug development and mode of action of the drugs. Bovine serum albumin (BSA) is the most extensively studied serum albumin, due to its structural homology with human serum albumin (HSA) [34]. The three amino acid residues tryptophan, tyrosine and phenylalanine in Bovine Serum Albumin (BSA) have fluorescence properties, and so BSA emits when excited. The relative ratio of fluorescence intensity for these three amino acids residues is 100:9:0.5, and thus the intrinsic fluorescence intensity of BSA when excited at 295 nm mainly come from the tryptophan residues, Trp-134 and Trp-212 embedded in subdomain IB and subdomain II A (Fig 3(b)).

The interaction of **1–10** with serum albumins has been studied by tryptophan emission-quenching experiments. BSA solutions exhibit a strong fluorescence emission with a peak at 343 nm due to the tryptophan residues, when excited at 295 nm [35]. The changes in the emission spectrum of tryptophan in BSA are primarily due to change in protein conformation, subunit association, substrate binding or denaturation [34]. complexes **1–10** in buffer solutions did not exhibit any emission spectra under the same experimental conditions. Addition of complexes **1–10** (0-10μM) to BSA (6.6 μM) resulted in a significant decrease of the fluorescence signal for BSA (λ_{max}=343 nm) (Fig. 3.13), due to possible changes in protein secondary structure of BSA indicating the binding of the compounds to BSA. It was observed that the complexes showed more % fluorescence quenching compared to the ligands (LFL/MFL) indicating stronger protein binding of the drugs on complexation.

The values of the Stern-Volmer quenching constants and the quenching rate constants for the complexes **1-10** interacting with BSA are calculated by Stern-Volmer quenching equation (3.1) [36] and the corresponding Stern-Volmer plots Io/I versus $[Q]$ (Fig. 3.14):

$$\frac{I_o}{I} = 1 + K_{SV}[Q] = 1 + k_q\tau_0[Q] \quad \text{.....(3.1)}$$

Where I_o is the initial tryptophan fluorescence intensity of BSA I is the tryptophan fluorescence intensity of BSA after the addition of the quencher, K_{SV} (M^{-1}) the quenching constant, kq ($M^{-1}s^{-1}$) the quenching rate constant, τ_0 the average fluorescence lifetime (10^{-8}s) [37] of BSA without the quencher, and $[Q]$ the concentration of the quencher. The quenching constants (K_{SV} M^{-1}) can be obtained from the slope of the plot Io/Iversus $[Q]$ and has been tabulated in Table 3.8.

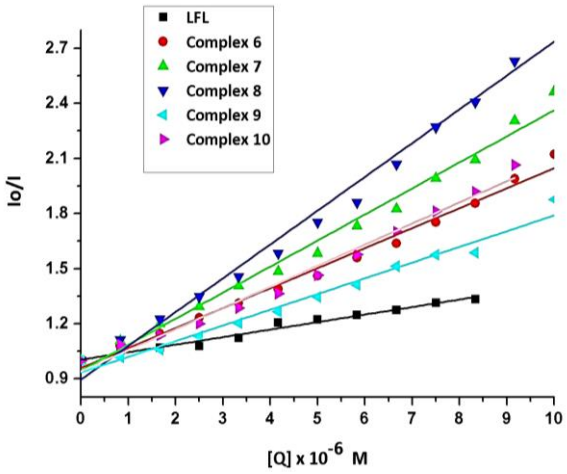

Fig 3.14: Stern–Volmer plot for the quenching of BSA fluorescence by complexes **6-10.**

The double-logarithm equation (3.2) [38] has been employed to determine the association binding constant (Ka) and n, the number of binding sites on BSA for ligand/complex- BSA interaction:

$$\log(Io-I)/I = \log Ka + n\log[Q] \quad \text{.....(3.2)}$$

The plot of $\log[(Io-I)/I]$versus $\log[Q]$ for each of the compounds is linear and the values of Ka and n have been obtained from the intercept and slope, respectively (Table 3.8).

The calculated values of K_{SV} (quenching constant) and kq (quenching rate constant) for the interaction of LFL/MFL and complexes **1–10** with BSA (Table 3.8) indicate good BSA binding propensity of the complexes. Considering the Stern-Volmer constant of

about $10^5\ M^{-1}$ and the lifetime of albumins, 10^{-8}s, we obtain a value of $10^{13}\ M^{-1}s^{-1}$ for the rate constant (kq) of the bimolecular quenching process, which largely overrides the accepted limit of the rate constant ($2\times10^{10}\ M^{-1}s^{-1}$) of the diffusional quenching implying biopolymers. This observation supports the fact that the experimental quenching of albumin fluorescence is due to a predominantly static process.

Table 3.8: Quenching constant K_{SV}, quenching rate constant kq, association binding constant K_a and number of binding sites n for the interaction of Complex **1-10** with BSA.

Compound	Ksv	Kq $M^{-1}s^{-1}$	Ka	*n* No of binding sites
MFL	1.0×10^5	1.0×10^{13}	$1.92\text{x }10^4$	0.928
Complex 1	3.1×10^6	3.1×10^{14}	$7.28\text{x}10^5$	1.08
Complex 2	2.1×10^6	2.1×10^{14}	$6.89\text{x}10^5$	1.06
Complex 3	8.5×10^6	8.5×10^{14}	$8.92\text{x}10^6$	1.09
Complex 4	2.0×10^6	2.0×10^{14}	$5.76\text{x}10^5$	1.04
Complex 5	1.5×10^6	1.5×10^{14}	$4.84\text{x}10^5$	1.12
LFL	$4.0\text{x }10^4$	$4.0\text{x }10^{12}$	$1.01\text{x }10^4$	0.884
Complex 6	$1.84\text{x }10^5$	$1.84\text{x }10^{13}$	$9.98\text{x}10^5$	1.12
Complex 7	$1.44\text{ x }10^5$	$1.4\text{ x }10^{13}$	$9.28\text{x}10^4$	1.04
Complex 8	$2.08\text{ x }10^5$	$2.08\text{ x }10^{13}$	$6.49\text{x}10^4$	1.06
Complex 9	$1.15\text{x }10^5$	$1.15\text{x }10^{13}$	$3.02\text{x}10^6$	1.09
Complex 10	$8.55\text{x }10^4$	$8.55\text{x }10^{12}$	$2.7\text{x}10^7$	1.49

3.4.5.1 Isothermal Calorimetry

Representative calorimetric titration of complex **6** (3.1×10^{-3} M) with BSA (0.09×10^{-3}M) in the presence of phosphate buffer at pH 7.0 is shown in Fig. 3.15(a). Each peak in the binding isotherm represented a single injection of the complex into BSA solution. Integration of the area of cell feedback by subtracting the heats of dilution of both the metal complex and protein gave the differential curve given in Fig. 3.15(b). The amount of heat generated per injection has been shown as a function of number of injections. A model of two independent sites fitted adequately to the calorimetric data. The smooth solid line shown in Fig. 3.15(b) was the best fit to the experimental data represented by square symbols, according to two independent binding site models. The model with a single binding site or three independent binding sites did not fit the experimental data. The thermodynamic parameters accompanying the binding of complexes to BSA are summarized in table 3.9. Since phosphate has a small value of the enthalpy of ionization (3.6 $KJmol^{-1}$), the observed values of enthalpy were practically the binding enthalpies of the complexes to the protein. As the titration progressed, the area under the peaks progressively became smaller due to an increased occupancy of binding sites on BSA with complex molecules.

Association binding constants K_I and K_{II} for site I and site II respectively were comparable for LFL and complex **7**, indicating that these compounds have similar binding affinities for either of the sites (Table 9). Complex **6** binds to site I ($K_I = 10^7$) much more strongly compared to site II ($K_{II} = 10^4$) whereas **8**, **9** and **10** have stronger binding affinities for site II. The integrated heat profiles showed that binding of complexes **6-10** to BSA were exothermic process. The observed exothermicity suggested a predominant involvement of electrostatic interactions in the binding process, however possibility of hydrophobic and H-bond interactions could not be ruled out [39]. Binding of complexes at site I seemed to be driven primarily by an entropic

contribution, ΔS values contributed favourably to the free energy of binding, indicating a strong hydrophobic interaction in the binding process [39]. The presence of aromatic rings provided significant hydrophobic character to the complexes and possibility of hydrophobic interactions with the binding site on the protein. In contrast, binding to site II was either enthalpy driven (**7** and **10**) suggesting electrostatic interactions, or entropy driven (**6** and **8**) or both enthalpy and entropy driven (**9**). The unfavourable entropy observed in some complexes most likely arises due to the ligand binding and reorientation of the solvent structure to a different extent.

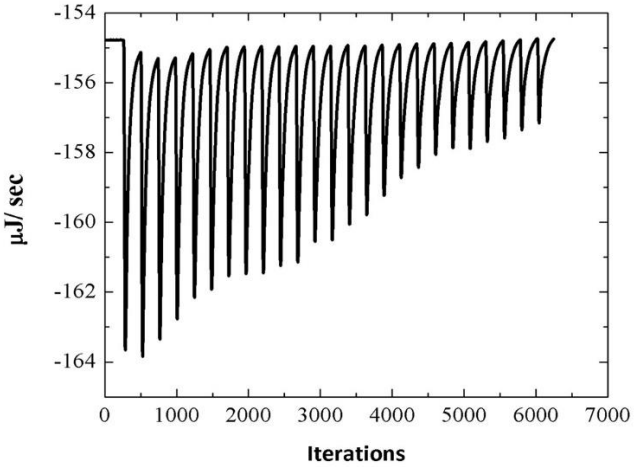

Fig 3.15 a. Titration of complex **6** (3.1 x 10^{-3} M) with BSA (0.09x10^{-3}M) at pH 7.0 and 298.15 K, showing the calorimetric response as successive injections of ligand are added to the reaction cell.

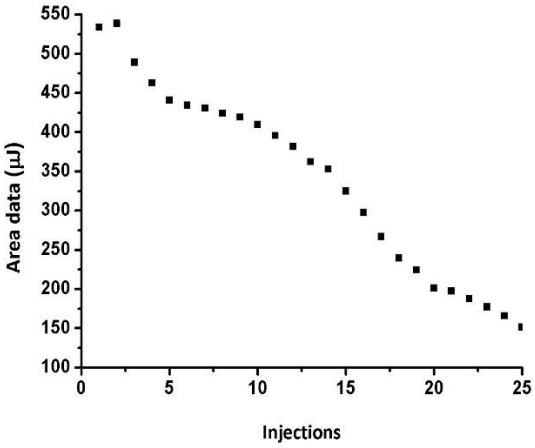

Fig 3.15 b. Modelling data for set of 2 independent site model. (graphs shows amount of heat released per injection)

Table 3.9: Binding Affinities K, Enthalpies ΔH and Entropies ΔS, accompanying binding of complexes **1-5** to BSA at site I and II at temperature 298 K and pH 7.0

Compound	K_I	ΔH_I KJ mol^{-1}	ΔS_I	K_{II}	ΔH_I KJ mol^{-1}	ΔS_I
LFL	2.68 x 10^4	-179.8	-0.51	2.67 x 10^4	189.8	-0.71
Complex 6	3.87 x 10^7	5.63	0.16	3.28 x 10^4	60.54	0.21
Complex 7	5.13 x 10^8	189.1	0.80	3.28 x 10^8	-142.3	-0.31
Complex 8	1.63 x 10^4	95.03	0.39	9.90 x 10^4	21.24	0.16
Complex 9	1.16 x 10^3	182.63	0.67	8.98 x 10^5	-0.87	0.11
Complex 10	1.05 x 10^4	102.6	0.42	1.00 x10^5	-136.2	-0.39

3.4.6 Cytotoxicity studies

3.4.6.1 MTT assay

MTT assay has been carried out to determine the cytotoxicity of complexes 1-10 on A549 human lung cancer cell line. MTT is a tetrazolium dye that measures mitochondrial dehydroganase activity as an indicator of cell viability.

The cytotoxic effect of the complexes were examined on cultured A549 human lung cancer cells by exposing cells for 12 h to a medium containing **1-10** at 5-94.5 μg/ml concentration (Fig. 3.16). All the complexes inhibited the growth of the cancer cells significantly, in a dose- and time-dependent manner. The cytotoxic activity was determined according to the dose values of the complexes required to reduce survival to 50% (IC_{50}), compared to untreated cells. The IC_{50} values are given in Table 3.10. A cursory glance over the performance of all complexes revealed that **3** showed maximum cytotoxicity as compared to other metal complexes investigated herein. It is suggested that the extent of interaction of complexes with DNA is related to their cell killing ability. DNA cleaving ability is an imperative credential for manifesting anti-cancer potential. Studies on serum protein binding assays conducted by other research groups [40] have inferred that antitumor metallo-drugs form protein-bound complexes, possibly inhibiting fundamental enzyme functions of cancer cells. Therefore; high magnitude of cytotoxicity observed in complex **3** is attributable to its strong DNA binding, DNA cleaving and/or protein binding propensity.

Table 10 : IC_{50} values of complexes **1–10** obtained from MTT assay on A549 cells.

Compounds	MFL	1	2	3	4	5	LFL	6	7	8	9	10
IC_{50} µg/ml	52.5	8.2	12.4	6.0	47.2	18.1	84.3	15.2	18.1	11.0	55.0	24.8

(A)

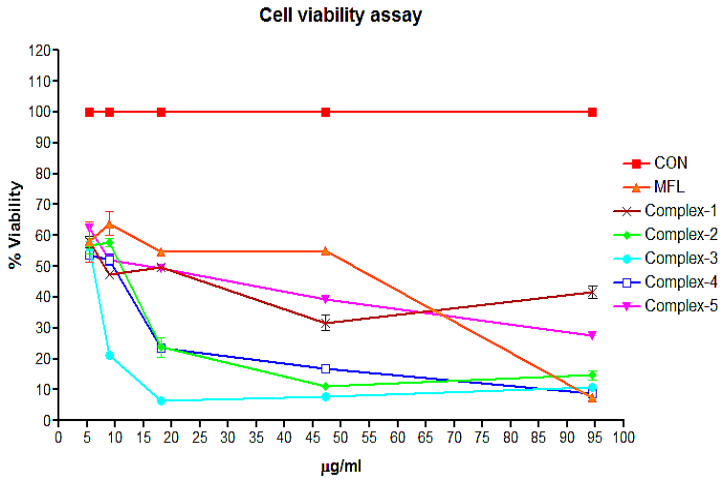

(B)

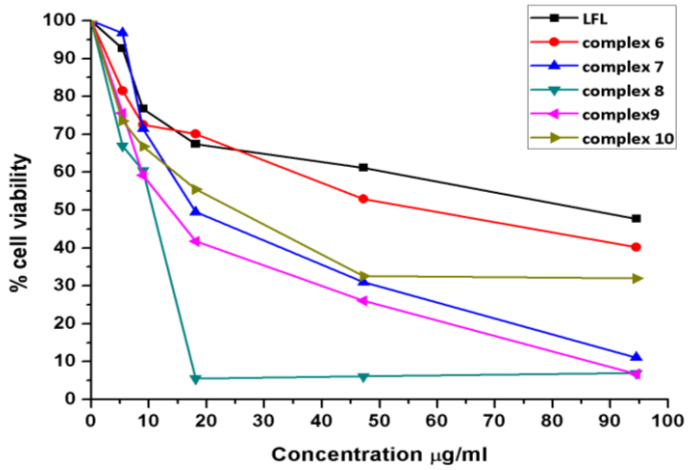

Fig 3.16. % cell viability in presence of (A) complexes **1-5** and (B) complexes **6-10** for A549 human lung cancer cell lines. Each point is the mean±standard error obtained from three independent experiments.

3.4.6.2 Alterations in cell morphology

The cytotoxicity caused due to the exposure of A-549 cell line to **1-10** was further assessed under phase contrast microscope (Fig. 3.17). Control cells appeared to be healthy with eccentric and occasional multiple nucleoli and relatively less cytoplasmic content. However, treatment with **1-10** (IC_{50} values) induced significant morphological alterations wherein, cells appeared to be round and shrunken. The overall flattened appearance of cells treated with complexes is possibly due to surface modifications that possibly manifest changes in adherent property of the cells. Multinucleated giant cells suggest inhibition of cytokinesis and some cells showed these characteristics following treatment with **1-10.** Also, evidences of cell surface blebbing, an early feature of apoptosis could be observed here.

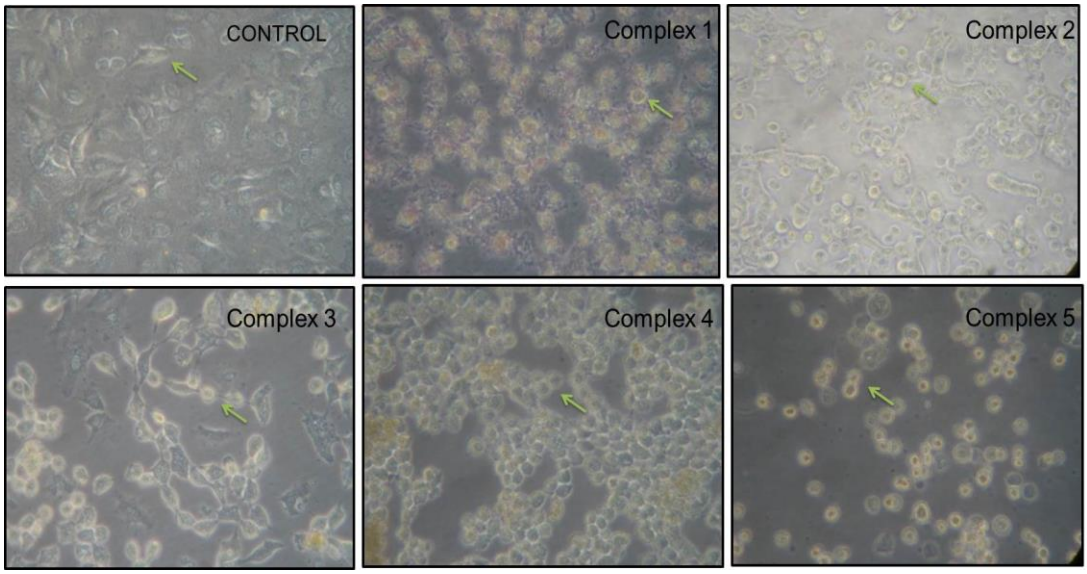

Fig 3.17: A-549 cells observed under phase-contrast microscope before and after treatment with complexes.

3.4.6.3 AO/EB staining

Cell death can be divided into two types: necrosis (accidental cell death) and apoptosis (programmed cell death). Necrotic cells undergo cell lysis and lose their membrane integrity, and severe inflammation is induced [41]. Apoptotic cells, however, are transformed into small membrane-bound vesicles (apoptotic bodies) which are engulfed in vivo by macrophages, and no inflammatory response is found [42]. Harmless removal of cells (cancer cells, for example) is desired in chemotherapy. Therefore, induction of apoptosis is one of the considerations in the development of anticancer drugs.

The type of cell death induced by complexes was investigated by the apoptosis assays-acridine orange/ethidium bromide (AO/EB) staining. The AO/EB staining assay can detect the difference in membrane integrity between necrotic and apoptotic cells [43]. AO is a vital dye and can stain both live and dead cells. EB stains only cells that have lost their membrane integrity. Under the fluorescence microscope, live cells appear green. Necrotic cells stain red, but have a nuclear morphology resembling that of viable cells. Apoptotic cells appear green and morphological changes such as cell blebbing and formation of apoptotic bodies are observed.

Microphotographs of AO/EB stained A549 cells, which were pre-treated for 12 h with **1-10**, showed that all the complexes induced apoptosis. Complex **3** is found to be more effective in inducing apoptosis, as higher numbers of condensed nuclei are observed in A549 cells after 12 h (Fig 3.18). The results suggested that **1-10** caused predominantly apoptosis of A549 cells.

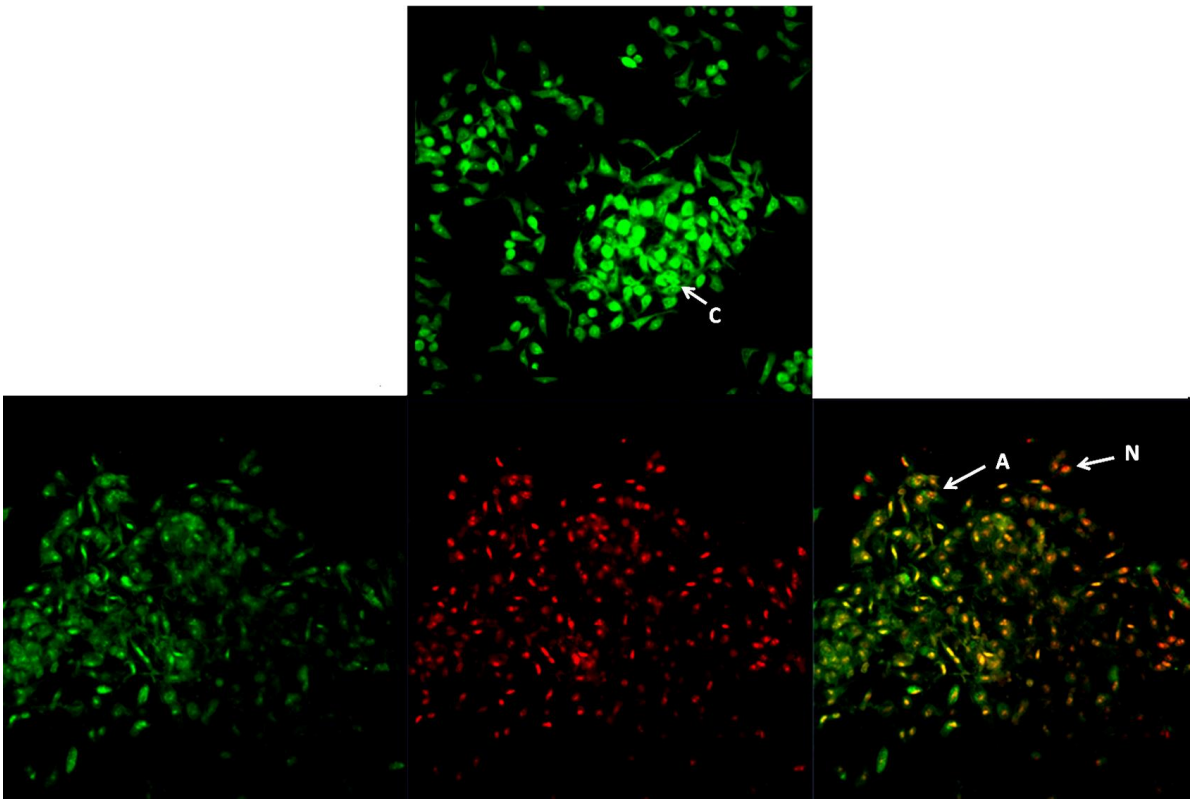

Fig 3.18. Microphotographs of A549 cells were stained by AO/EB and observed under confocal microscope: (C) A549 cell without treatment; (1) in the presence of complex **3**; incubated at 37˚ C and 5% CO_2 for 12h. Arrows point to the cells representing certain cell viable status: A, the apoptotic cells; and N, the necrotic cells.

3.4.6.4 Dapi staining

DAPI (4′, 6-diamidino-2-phenylindole) is a fluorescent dye that binds strongly to A–T rich regions in DNA and produces blue florescence at excitation wavelength 358 nm and emission wavelength 461 nm. In order to detect early onset of apoptotic changes, DAPI staining is adopted to assess gross changes in the nuclear morphology [44].

After treatment with **1-10** at their respective IC_{50} concentrations for 12 h the cells were observed for cytological changes adopting dapi staining. The observations revealed that all the complexes brought about marginalization and/or fragmentation of chromatin, bi-nucleation, cytoplasmic vacuolation, nuclear swelling, cytoplasmic blebbing and late apoptosis indication of dot-like chromatin and condensation in the A549 human lung

cancer cells (Fig. 3.19). These cytological changes indicate that the cells were committed to specific mode of cell death, apoptosis.

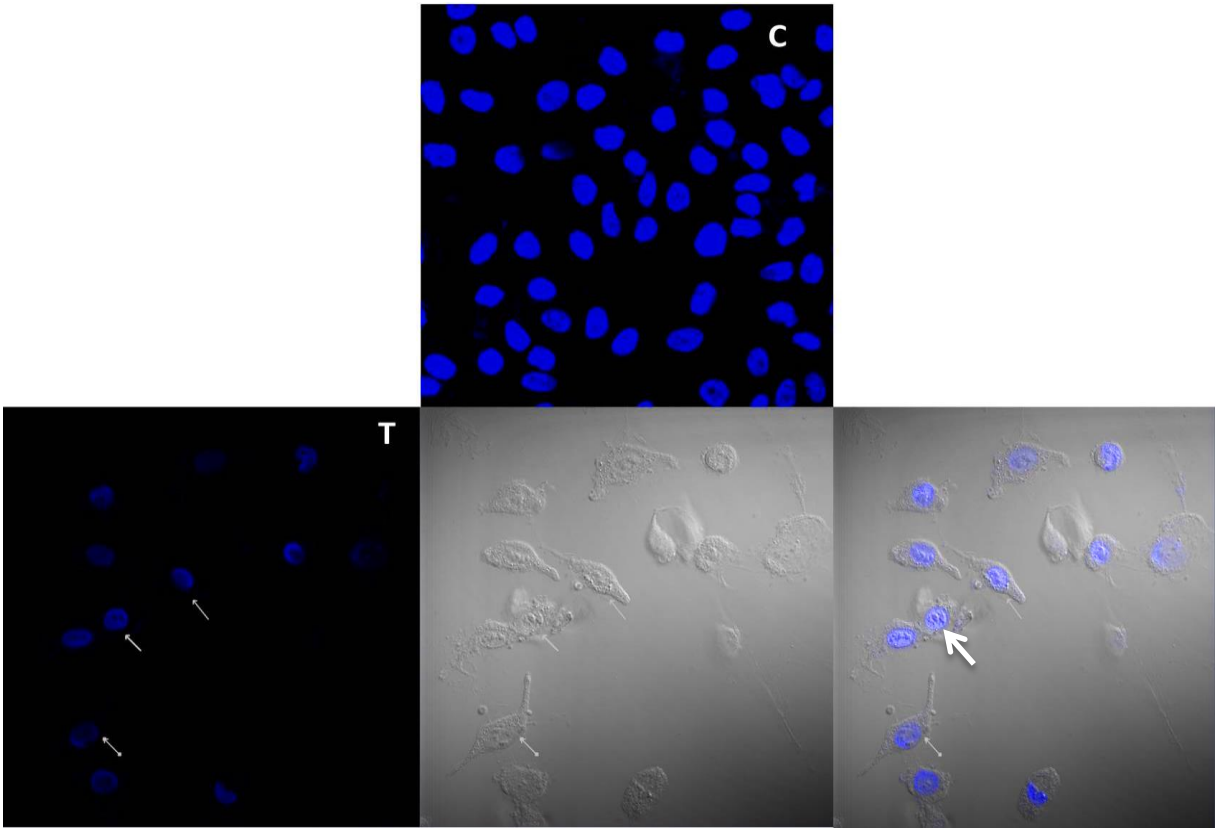

Fig 3.19. Microphotographs of A549 cells were stained with Dapi and observed under confocal microscope: (C) A549 cell without treatment; (1) in the presence of complex **3**; incubated at 37˚ C and 5% CO_2 for 12h.

3.4.6.5 Intracellular ROS generation and oxidative stress

Free radicals or reactive oxygen species (ROS) are involved in the regulation of many physiological processes. However when ROS production increases (cellular or external) and overwhelms the cellular antioxidant capacity, it can induce macromolecular damage (by reacting with DNA, proteins, and lipids) and thus contributes to a broad spectrum of diseases and pathological conditions. In the first instance, damage can lead to apoptosis or necrosis. DCFDA (2',7'-dichlorofluorescein diacetate) is a cell permeable fluorescent dye that measures hydroxyl, peroxyl, and other ROS activities within the cell. After diffusion into the cell, DCFDA is deacetylated by cellular esterases to a nonfluorescent compound, which is later oxidized by ROS into 2',7'-dichlorofluorescein (DCF), a highly fluorescent dye.

In the present study, the images taken using fluorescence microscopy of A549 cells treated with complexes **1-10** at IC_{50} concentration for 12 h, revealed prominent green fluorescence. Cells were distinctly stained with the DCFDA dye indicating excessive ROS generation, whereas the control cells were faintly stained by the dye or not stained at all (Fig. 3.20). The ability of complexes **1-10** in generating intra cellular ROS can be correlated with their ability to oxidatively cleave DNA as discussed earlier. Increase in intracellular oxidative stress caused rapid depletion of cellular antioxidants thus rendering the cell to further structural and functional damages and the same is noted herein following treatment with complexes **1-10**.

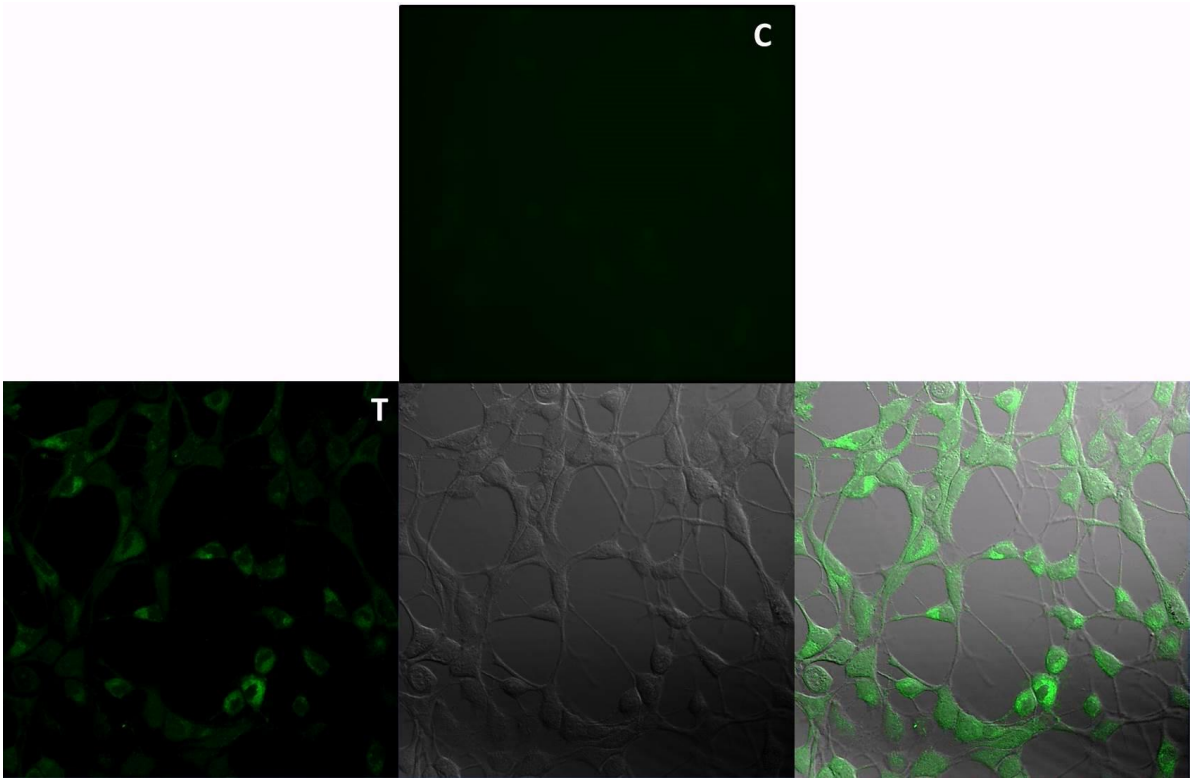

Fig 3.20: Microphotographs of A549 cells were stained with DCFDA and observed under confocal microscope: (C) A549 cell without treatment; (1) in the presence of complex **3**; incubated at 37˚ C and 5% CO_2 for 12h.

3.4.6.6 Assessment of DNA damage

The formation of oligo-nucleosomal DNA fragments were assessed using an electrophoretic technique called "DNA ladder" that reveals a visual profile of DNA damage**.** The results presented in Fig. 3.21 showed that the LFL/MFL ligands also provoke DNA fragmentation in A-549 cells, though the phenomenon was very weak and took place after longer incubation (24 h) compared to the one observed in case of complexes **1-10,** after 12 h incubation (Fig. 3.21) implying that the metal complexation enhanced the apoptotic effect of the fluoroquinolone drugs in A-549 cells.

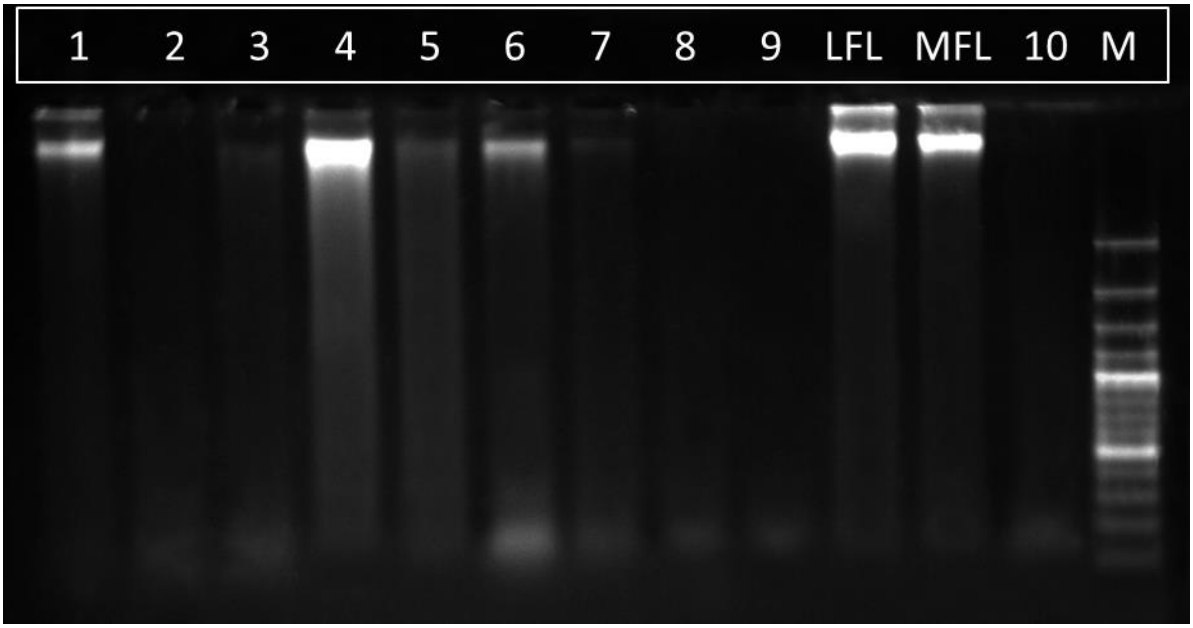

Fig 3.21: Photogenic view of cleavage of A-549 cells with series of complexes **1-10** using 1.5% agarose gel containing ethidium bromide. All complexes were incubated for 16 h at 37 °C. Lane 1, complex **1**; Lane 2, complex **2**; Lane 3, complex **3**; Lane 4, complex **4**; Lane 5, complex **5;** Lane 6, complex **6**; Lane 7complex **7**; Lane 8, complex **8**; Lane 9, complex **9**; Lane 10, **MFL**; Lane 11,**LFL**; Lane 12, complex **10**; Lane 13, **Marker.**

3.4.6.7 Influence of metal complexes on apoptotic and anti-apoptotic gene

Expression levels of pro-apoptotic and anti-apoptotic genes (BAX and Bcl-2 respectively) were assessed on A-549 (Human Lung Carcinoma) by a 12 h exposure of complexes **6-10** to the cancer cells. Results (Fig. 3.22) revealed that expression of BAX notably increased after treatment with complexes **6**, **9** and **10** suggesting that they possibly have capacity to trigger apoptotic pathway and cause death of cancer cells. These results were also in agreement with the MTT assay. Alternatively expression levels of Bcl-2 in A-549 cells treated with complexes **6, 9** and **10** were low further suggesting higher vulnerability for trigger of apoptosis. In contrast A-549 cells treated with complexes **7** and **8** showed increased Bcl-2 expression and lower BAX expression indicating that these complexes were less efficient in causing apoptosis of the cancer

cells, since higher level of Bcl-2 expression indicates lowered apoptosis. These results provide valuable evidence on the role of metal complexes (**6, 9** and **10**) in triggering apoptosis in cancer cells (A-549) and indicate at merits of these metal complexes as potent anticancer agents.

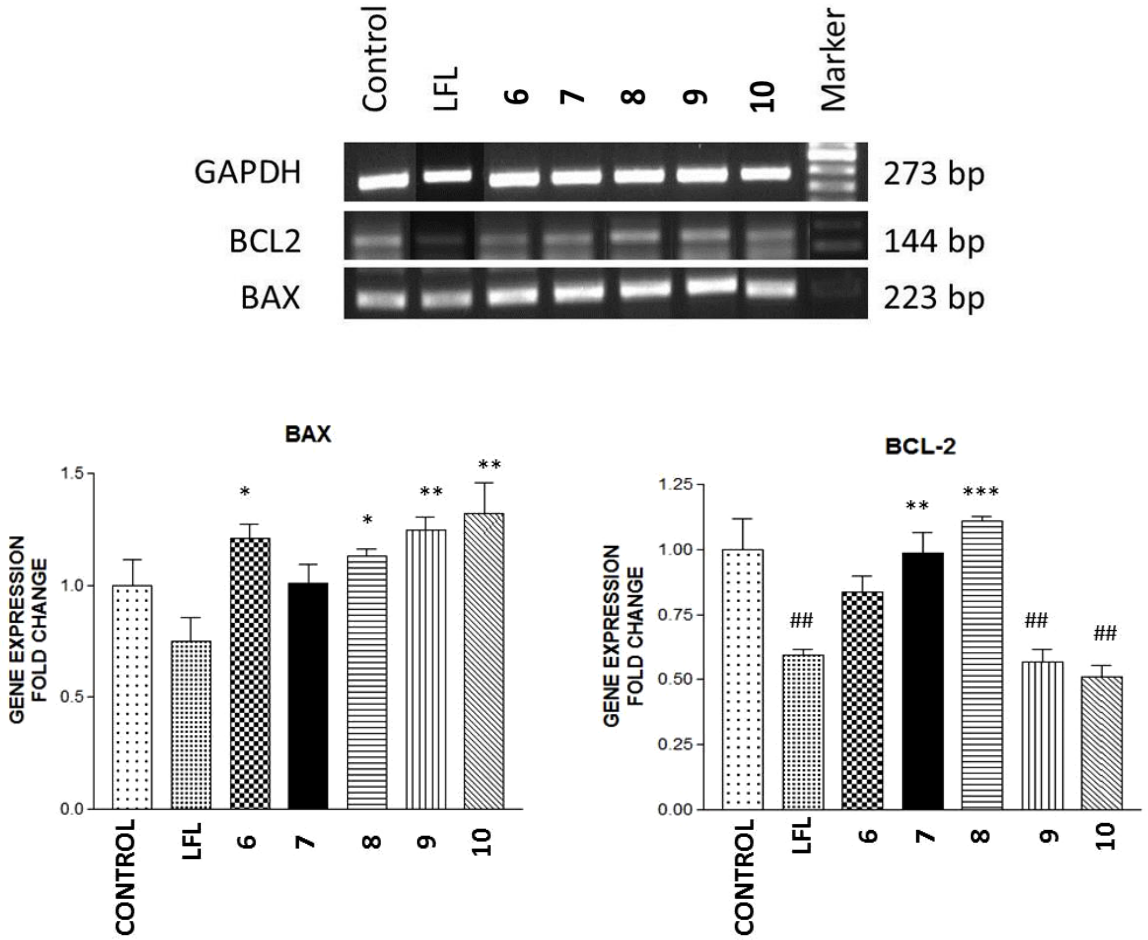

Fig 3.22 : RT PCR analysis was done to detect apoptotic gene expression (BAX) and also levels of anti-apoptotic gene (BCL-2). Bands were detected using Gel Doc (Biorad). Data was analysed by using Image J software. GAPDH was used as internal control. Values are mean ± SEM from three independent experiments. *0 represents P<0.05, ** represents P<0.01, ***represents P<0.001 while comparing with standard MO and ## represents p<0.01 while comparing with control.

3.5 Conclusion

The synthesis and characterization of 10 mononuclear complexes of the third-generation fluoroquinolone antibacterial drugs moxifloxacin (MFL) and levofloxacin (LFL) with the ions Fe^{3+},Cu^{2+},VO^{2+},Mn^{2+},$Ni^{2+}$and Zn^{2+} has been achieved with physicochemical and spectroscopic methods. In the complexes, fluoroquinolones are in zwitterionic form and act as bidentate ligands coordinated to metal (II/III) ions through the pyridone oxygen and a carboxylato oxygen. Binding of these complexes with CT-DNA was investigated by spectroscopic, electrochemical and viscometric techniques. It suggested that the complexes have good binding affinity for CT- DNA via intercalative mode with the Cu^{2+}complex exhibiting the highest K_b value. Artificial nuclease activity has been ascertained by gel electrophoretic mobility assay; the complexes displayed efficient cleavage activity of DNA converting Form I to Form II and ultimately leading to the formation of linearized Form III. The interactions of the complexes with bovine serum albumin have been studied by fluorescence spectroscopy revealing their good binding affinity to BSA with high binding constants. The complexes exhibited higher binding affinity (Ka values) than the free quinolones.

The anticancer activity of the complexes on A549 (human lung cancer) cell line has been studied. In vitro, the complexes exhibited higher cytotoxicity than the quinolone drugs and induced apoptosis in A-549 cells by DNA damage in a dose dependent manner as revealed by AO/EB staining. All the complexes were found to promote DNA fragmentation in lung cancer cells A-549 and reactive oxygen species were responsible for cleavage. Gene expression analysis results revealed complexes **6, 9** and **10** upregulated the levels of the proapoptotic proteins BAX and downregulated the levels of the antiapoptotic proteins Bcl-2, in A-549 cells. These results indicate that the synthesized complexes induce apoptosis of A-549 cells through activation of caspases and ROS mediated mitochondrial dysfunction pathways. In summary, we present series

of transition metal complexes of fluoroquinolone drugs (MFL/LFL), displaying strong DNA/BSA binding, DNA cleavage and cytotoxic activity. These results could be of importance towards the designing and developing metal complexes as potential agents capable of interacting at the specific site of DNA and protein for their use as artificial nucleases and proteases.

References

[1] http://www.cancer.org/Cancer/LungCancer-Non SmallCell/ Detailed Guide /nonsmall-cell-lung-cancer-key-statistics; (2012-4-3).

[2] B. Joseph, D. Marchetti, P. Formstecher *etal* Oncogene., 21 (2002) 65.

[3] Z .Guo, P. Sadler, Angew. Chem., Int. Ed. Engl., 38 (1999) 1512.

[4] B. Lippert, Coord. Chem. Rev., 487 (2000) 200.

[5] J. M. Domagala, L. D. Hanna, C. L. Heifetz, M. P. Hutt, T. F Mich, J. P. Sanchez, and M. Solomon, J. Med.Chem., 29 (1986) 394.

[6] D. H. Kang, J. S. Kim, M. J. Jung, E. S. Lee, Y. Jahng, Y. Kwon, and Y . Na, Bioorg. Med. Chem. Lett., 18 (2008) 1520.

[7] M. Paul, A. Gafter-Gvili, A. Fraser, and L. Leibovici, Eur. J. Clin. Microbiol. Infect. Dis., 26 (2007) 825.

[8] J. Robles, J. Martin-Polo, L. Varez-Valtierra, L. Hinojosa, G. Mendoza-Diaz, Met. Based Drugs., 7 (2000) 301.

[9] I.Turel, Coord. Chem. Rev., 232 (2002) 27.

[10] A.S. Wagman, M.P. Wentland, Comprehensive Medicinal Chemistry II. 7(2007) 567.

[11] Margarete MS. Heck, William C. Earnshaw The journal of cell biology.,103 (1986) 2569.

[12] V.T. Andriole, Clin. Infect. Dis., 41 (2005) 113.

[13] K.E. Brighty, T.D. Gootz, in: V.T. Andriole (Ed.), The quinolones, Academic Press, San Diego, (2000) 34.

[14] Nakamoto K, (1986) Infrared and Raman Spectra of Inorganic and Coordination Compounds, fourth ed., Wiley, New York.

[15] M.C, Jain, A.K, Srivastava, P.C. Jain, Inorg. Chim. Acta., 23 (1977) 199.

[16] B.J. Hathaway, D.E. Billing, Coord. Chem. Rev., 5 (1970) 143.

[17] T.S. Smith, R. LoBrutto, V.L. Pecoraro, Coord. Chem. Rev., 228 (2002) 1.

[18] T.D. Thangadurai, S.K Ihm, J. Ind. Eng. Chem., 9 (2003) 563.

[19] K. E. Erkkila, D. T. Odom, J. K Barton, Chem. Rev., 99 (1999) 2777.

[20] J.K. Barton, A.L. Raphael, J. Am. Chem. Soc., 106 (1984) 2172–2176.

[21] H. Chao, W. Mei, Q. Huang, L. Ji, J. Inorg. Biochem., 92 (2002) 165.

[22] E.C. Long, J.K. Barton, Accounts Chem. Res., 23 (1990) 271.

[23] A.M. Pyle, J.P. Rehmann, R. Meshoyrer, C.V. Kumar, N.J. Turro, J.K. Barton, J. Am. Chem. Soc., 111 (1989) 3053.

[24] S. Dhar, M. Nethaji, A.R. Chakravarty, J. Inorg. Biochem., 99 (2005) 805.

[25] Y. Wang, H. Zhang, G. Zhang, W. Tao, S. Tang, J. Lumin., 126 (2007) 211.

[26] F. Dimiza, S. Fountoulaki, A.N. Papadopoulos, C.A. Kontogiorgis, V. Tangoulis, C.P. Raptopoulou, V. Psycharis, A. Terzis, D.P. Kessissoglou, G. Psomas, Dalton Trans. 40 (2011) 8555.

[27] H. Halliwell, Lancet., 344 (1994) 721.

[28] P. Wittung, P.Nielsen, B. Norden, J. Am. Chem. Soc., 118 (1996) 7049.

[29] U. Maheswari P, M Palaniandavar, J. Inorg. Biochem., 98(2004) 219.

[30] P. Lincoln, E. Tuite, B. Norden J. Am. Chem. Soc., 119(1997) 1454.

[31] B. Norden, F. Tjerneld, Biopolymers., 21(1982) 1713.

[32] M.T. Carter, A.J. Bard ,J.Am. Chem. Soc., 109 (1987) 7528.

[33] C.K. Skyrianou, E.K. Efthimiadou, V. Psycharis, A.Terzis, D.P. Kessissoglou, G. Psomas, Journal of Inorganic Biochemistry., 103(2009) 1617.

[34] Y. Wang, H. Zhang, G. Zhang, W. Tao, S. Tang, J. Lumin., 126 (2007) 211.

[35] C. Andre, Y.C. Guillaume, J. Chromatogr. B., 801 (2004) 221.

[36] Y. Hu, Y. Liu, J. Wang, X. Xiao, and S. Qu, Journal of Pharmaceutical and Biomedical Analysis., 36 (2004) 915.

[37] J. R. Lakowicz and G. Weber, Biochemistry., 12 (1973) 4161.

[38] B. Ahmad, S. Parveen, and R. H. Khan, Biomacromolecules., 7 (2006)1350.

[39] N. Keswani, S. Choudhary and N. Kishore, J. Biochem., 148(1) (2010) 71.

[40] RT. Andrei, G.H.Christian, S.A. Svetlana, K.K. Bernhard, Chem Rev., 106 (2006) 2224.

[41] R. Van Furth, T.L. Van Zwet, J. Immunol. Methods., 108 (1988) 45.

[42] J.S. Savill, P.M. Henson, J.E. Henson, C. Haslett, M.J. Walport, A.H. Wyllie, J. Clin. Invest., 83 (1989) 865.

[43] G.P. Amarante-Mendes, E. Bossy-Wetzel, T. Brunner, D. Finucane, D.R. Green, S. Kasibhatla, in: D.L. Spector, R.D. Goldman, L.A. Leinwand (Eds.), Cells: Laboratory Manual, Vol. 1, Cold Spring Harbor Laboratory Press, New York, (1998)(Chapter 15).

[44] A.T. Farial, M.V. James, B. Henryk, S.R. Lynda, W. David, Biochemistry., 31(1992) 3103.